THESIS FOR THE DEGREE OF DOCTOR OF PHILOSOPHY

# *Particle motion, coating and drying in Wurster fluidized beds*

## *- An experimental and discrete element modeling study*

---

**LIANG LI**


Chemical Engineering

Department of Chemistry and Chemical Engineering

CHALMERS UNIVERSITY OF TECHNOLOGY

Gothenburg, Sweden 2015

**Particle motion, coating and drying in Wurster fluidized beds - An experimental and discrete element modeling study**

LIANG LI

ISBN: 978-91-7597-251-0



Doktorsavhandlingar vid Chalmers tekniska högskola

Serie Nr 3932

ISSN 0346-718X

Department of Chemistry and Chemical Engineering

Chalmers University of Technology

SE-412 96 Gothenburg, Sweden

Telephone +46(0)31-772 1000

Printed by Chalmers Reproservice

Gothenburg, Sweden 2015

Cover: The cover image shows a DEM-CFD simulation of particle motion in the LAB CC system. The particles are colored by their vertical velocity, and the central plane is colored by air velocity. The red color represents a high value, and the blue color represents a low value. The shadow illustrates the walls of the fluidized bed and the Wurster tube, and the grid used.

# Particle motion, coating and drying in Wurster fluidized beds - An experimental and discrete element modeling study

Liang Li
Department of Chemistry and Chemical Engineering
Chalmers University of Technology
SE-412 96 Gothenburg, Sweden

## Abstract

This thesis focuses on developing a mathematical model that is capable of predicting the fluidized bed coating process. First a basic understanding of pellet motion in a Wurster fluidized bed was established by conducting a series of experiments using the positron emission particle tracking (PEPT) technique. The PEPT results, such as the particle velocity, the cycle time distribution (CTD) and the residence time distribution (RTD) of particles in different regions of the fluidized bed, were selected to evaluate the model for pellet motion based on the discrete element method, computational fluid dynamics (DEM-CFD). In an effort to refine the sub-models involved in the DEM, the effects of the drag model were investigated. With the validated DEM-CFD model, the detailed pellet motion in the spray zone of the fluidized bed was studied. In order to identify the underpinning mechanisms by which coating thickness changes, pellets of different sizes were employed, and a simple model for predicting the growth of pellets was developed based on data available from the DEM-CFD results and the PEPT experiments. This predictive model was then evaluated experimentally. In addition, a model for drying of pellets was developed.

In the PEPT experiments, it was found that, for the parameters studied, particles spend approximately 12–29% of the cycle time in the Wurster tube. It was observed that particles tend to recirculate in the Wurster tube and sneak out from below the tube. In comparison with the PEPT experiments, the coupled DEM-CFD simulations showed close agreement with respect to the CTD and the RTD of particles in different regions. Using the validated DEM-CFD model, large particles were found to spend longer time in the spray zone and move closer to the spray nozzle. The latter effect provides evidence that large particles can shield small particles from spray droplets. Both of these effects suggest that large particles receive a greater amount of coating solution per particle cycle. A simple conceptual model was then developed to predict the effects of the residence time of particles in the spray zone, the particle cycle time, and the entrance distance on the relative rate of the increase in film thickness between large and small particles. By comparing predicted and measured relative rates of increase in coating thickness between large and small particles, it was confirmed that large particles grow faster than small particles.

***Keywords:*** *Fluidized bed, particle, coating, drying, airflow, DEM, CFD, PEPT, Wurster, spray*

# List of publications

The thesis is based on the following publications:

Paper I:

Li, L., Rasmuson, A., Ingram, A., Johansson, M., Remmelgas, J., von Corswant, C., & Folestad, S. (2015). PEPT study of particle cycle and residence time distributions in a Wurster fluid bed. *AIChE Journal, 61*(3), 756-768.

Paper II:

Li, L., Remmelgas, J., van Wachem, B. G. M., von Corswant, C., Johansson, M., Folestad, S., & Rasmuson, A. (2015). Residence time distributions of different size particles in the spray zone of a Wurster fluid bed studied using DEM-CFD. *Powder Technology, 280*(0), 124-134.

Paper III:

Li, L., Remmelgas, J., van Wachem, B. G. M., von Corswant, C., Folestad, S., Johansson, M., & Rasmuson, A. (2016). Effect of Drag Models on Residence Time Distributions of Particles in a Wurster Fluidized Bed: a DEM-CFD Study. *KONA Powder and Particle Journal,* 10.14356/kona.2016008.

Paper IV:

Li, L., Hjärtstam J., Remmelgas, J., von Corswant, C., Folestad, S., Johansson, M. & Rasmuson, A. (2015). Growth of differently sized particles in a fluidized bed coater. *Submitted to Powder Technology*.

Paper V:

Li, L., Remmelgas, J., van Wachem, B. G. M., Hjärtstam J., von Corswant, C., Folestad, S. & Rasmuson, A. (2015). A DEM-CFD study on drying of coated particles in a fluidized bed, *manuscript in preparation*.

# Contribution report

In addition to being the lead author in the above publications, the candidate has contributed in the following aspects to each paper below:

Paper I:

Prepared the experiments, analyzed the experimental data, and together with my co-authors, interpreted the results.

Paper II and III:

Performed the simulations, developed the code for pre- and post-processing, and together with my co-authors, interpreted the results.

Paper IV:

Performed the experiments with Hjärtstam J., analyzed the experimental data, and together with my co-authors, interpreted the results.

Paper V:

Performed the experiments with Hjärtstam J., carried out simulations and the analysis, developed the code for pre- and post-processing, and together with my co-authors, interpreted the results.

# Acknowledgements

This study was undertaken with financial support from the EU Seventh Framework Programme, AstraZeneca and Chalmers University of Technology.

First I would like to thank Anders Rasmuson and Staffan Folestad for giving me this unique opportunity to be involved in this exciting project. Thanks Anders for always being available and patient, for your motivation and guidance and for your encouragement. I would also like to thank Staffan for your broad view, knowledge and nice talks not only on the project but also on a variety of aspects.

Johan Remmelgas, as my co-supervisor and mentor, spent plenty of time and energy in helping me with problem solving, developing codes, examining and discussing results, writing and rewriting, as well as English. I appreciate all this very much. Many thanks to you.

To my co-supervisor Christian von Corswant, I am grateful for your valuable comments and for the insightful discussions we had.

I am also thankful to Berend van Wachem at Imperial College London for introducing me to MultiFlow and for remote but rewarding guidance and discussions.

I want to acknowledge Mats Johansson and Johan Hjärtstam for nice cooperation on the experimental work. In the experiments, I also received help from Bindhu Gururajan, Andy Ingram and Sven Karlsson, Anders Holmgren, Brita Sjöblom, Hanna Matic, Magnus Fransson, Livia Cerullo, Alvaro Diaz-Bolado; thank you all. During simulations, I received a lot of support from Mikael Bengtsson, Andreas Loong, Martin Budsjö and Nima Namaki at the high-performance computing (HPC) team, AstraZenceca; thank you very much.

To Lilia Ahrné, thank you for coordinating this beautiful network and organizing many wonderful events. To PowTech members, thank you very much for sharing during these years and it was really nice meeting you. In particular, it was great to have Duy Nguyen, Loredana Malafronte, Pooja Shenoy and Epameinondas Xanthakis in Gothenburg; I have fond memories of having beers, chats and dancing and traveling with you and David Valdesueiro.

I also enjoyed being the roommate of Kurnia Wijayanti; thank you for sharing relevant and irrelevant stories. Of course I am pleased to have friendly and helpful colleagues at Chalmers and AstraZeneca, who created an enjoyable working environment.

My special thanks go to my big brother Chaoquan Hu, Ms. Yan and their lovely son, Chengsong. May you succeed in achieving great happiness in the future!

Last but not least, I devote my deepest words to my beloved family and An'an: I love you!

“爸妈，晶晶，我爱你们，谢谢你们。因为有你们，让我懂得生命中什么是重要；因为有你们，让我有勇气面对一切；因为有你们，一切才变得有意义！你们都要好好的！”

# Contents

# Nomenclature

## Abbreviations

| | |
|---|---|
| CFD | computational fluid dynamics |
| CTD | cycle time distribution |
| DEM | discrete element method |
| EC | ethyl cellulose |
| EE | Eulerian-Eulerian |
| EL | Eulerian-Lagrangian |
| HPC | hydroxypropyl cellulose |
| IBM | immersed boundary method |
| FVM | finite volume method |
| LBM | Lattice-Boltzmann method |
| LES | large eddy simulation |
| MCC | microcrystalline cellulose |
| PEPT | positron emission particle tracking |
| PSD | particle size distribution |
| RHS | right hand side |
| RSD | relative standard deviation |
| RTD | residence time distribution |
| SEM | scanning electron microscope |
| TFM | two-fluid model |
| VMD | volume mean diameter |

## Roman letters

| | |
|---|---|
| A | area |
| B | inertial resistance coefficient |

| | |
|---|---|
| $c_p$ | specific heat capacity |
| $C$ | discharge coefficient |
| $C_D$ | drag coefficient |
| $d$ | diameter of the particle |
| D | pressure loss coefficient |
| $D_{AB}$ | diffusivity of the solvent in air |
| $D_s$ | aperture width |
| $E$ | Young's modulus |
| $\boldsymbol{F_c}$ | contact force |
| $\boldsymbol{g}$ | gravity |
| $h$ | convective heat transfer coefficient |
| $H$ | shear modulus |
| $H_{evp}$ | latent heat of evaporation |
| $I$ | the moment of inertia |
| $k$ | spring stiffness |
| $k_B$ | Boltzmann's constant |
| $k_{pg}$ | mass transfer coefficient |
| $l_{film}$ | thickness of the coating film |
| $l_p$ | thickness of the porous zone |
| $L$ | height of the spray zone |
| $m_p$ | particle mass |
| $m_p{}^*$ | effective particle mass |
| $\dot{m}$ | spray rate |
| $M$ | molar weight |
| $N_{cycle}$ | number of coating cycles |
| $N_i$ | degree of the polymerization, $i = 2$ |
| $N_{Re}$ | screen Reynolds number |
| $N_{w,p}$ | mass flux of liquid through the surface of the pellet |
| $P$ | pressure |
| PD | pressure drop through the wire mesh screen |

| | |
|---|---|
| $r$ | radius of the particle |
| $r_{entrance}$ | entrance distance |
| $Sc$ | Schmidt number |
| $Sh$ | Sherwood number |
| $R$ | gas constant |
| $Re$ | Reynolds number |
| $t$ | time |
| $t_{cycle}$ | cycle time |
| $t_{spray}$ | residence time in the spray zone |
| $T$ | temperature |
| $\boldsymbol{T}$ | torque |
| $\boldsymbol{u}$ | fluid velocity |
| $\boldsymbol{v}$ | particle velocity |
| $V$ | volume |
| $x$ | mole fraction of component |
| $Y$ | mass fraction |

**Greek letters**

| | |
|---|---|
| $\alpha$ | constant related to the coefficient of restitution |
| $\beta$ | interphase momentum transfer coefficient |
| $\varepsilon$ | volume fraction or porosity |
| $\delta$ | displacement of the particle |
| $\eta$ | damping coefficient |
| $\theta$ | spray half-angle |
| $\lambda$ | thermal conductivity |
| $\mu$ | friction coefficient |
| $\rho$ | density |
| $\sigma$ | Poisson's ratio |
| $\boldsymbol{\tau}$ | viscous stress tensor |

| | |
|---|---|
| $\phi$ | volume fraction of competent |
| $\boldsymbol{\omega}$ | rotational velocity |

**Subscripts**

| | |
|---|---|
| $g$ | gas phase |
| $i$ | the $i^{th}$ particle |
| $j$ | the $j^{th}$ particle |
| $n$ | normal direction |
| $p$ | particle |
| $sub$ | polymer substance |
| $t$ | tangential direction |
| $w$ | solvent |
| $1, 2$ | component $i$ |

# List of figures

# List of tables

# 1. Introduction

## 1.1. Background

Particle coating is a unit operation that is used in a variety of industries. For example, in the food industry, ingredients are coated to mask flavor or to improve stability and shelf life (Teunou & Poncelet, 2002). In the agricultural industry, seeds are coated to make them easier to handle, to allow them to be planted by machine, and to improve germination and crop yields (Filho *et al.*, 1998).

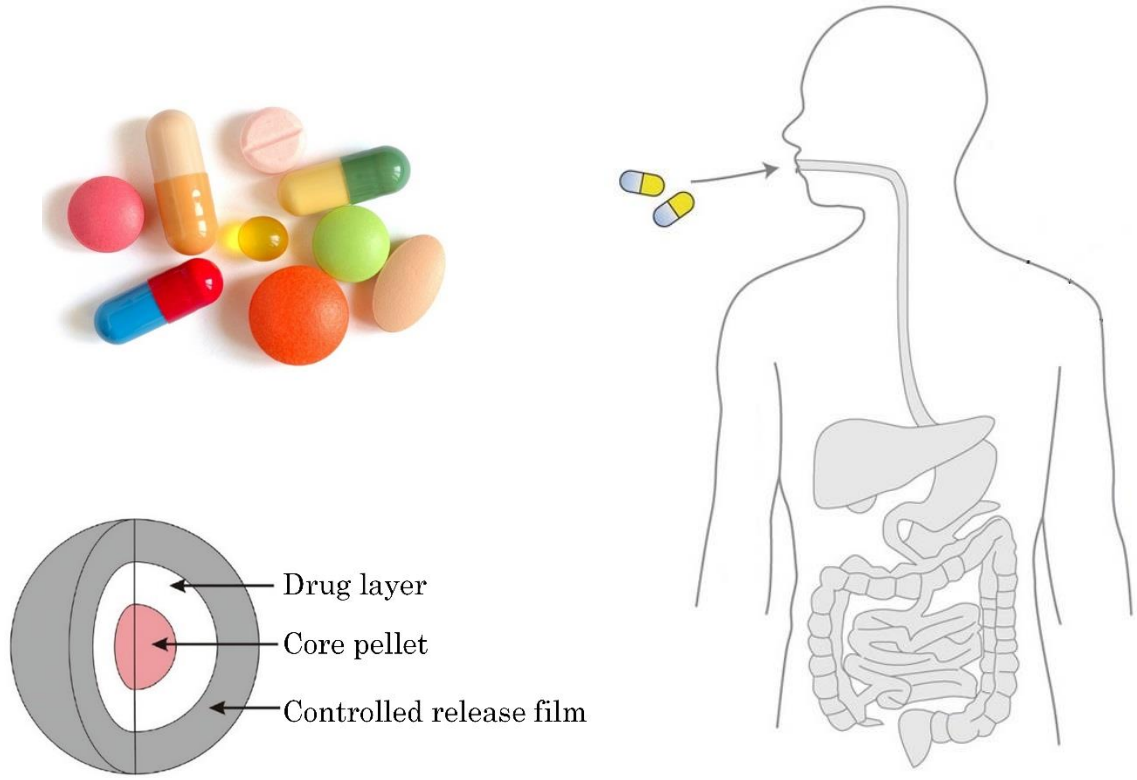


*Figure 1.1 Layout of a pellet and its usage, partly revised from the work of Kearney and Mooney (2013).*

In the pharmaceutical industry, which is the focus of this thesis, pellets are coated with drug substances and functional films, for example films for

controlled release (Jono *et al.*, 2000; Chopra *et al.*, 2002). In its simplest form, such a controlled-release pellet consists of, from inside to outside, a core pellet, a drug layer, and a controlled release film, as sketched in Figure 1.1. The core pellet can be made of sand, sugar, or cellulose while the controlled release film typically consists of a polymer or polymer blend that has been carefully selected to provide the desired drug release rate. When the patient swallows the medicine, the drug substance is released in the gastrointestinal tract and ultimately taken up in the blood. Preferably, the drug concentration in the blood should remain within a certain range that gives the desired therapeutic effects, i.e. the so-called therapeutic range. Without a mechanism that controls the rate of release of the drug substance, the drug concentration first rises and then decreases after reaching its highest level, as shown in Figure 1.2. In order to better control the drug release rate so that the drug concentration remains within the therapeutic range for a longer period of time, formulations that give sustained or extended drug release are developed, e.g. as shown in Figure 1.2.

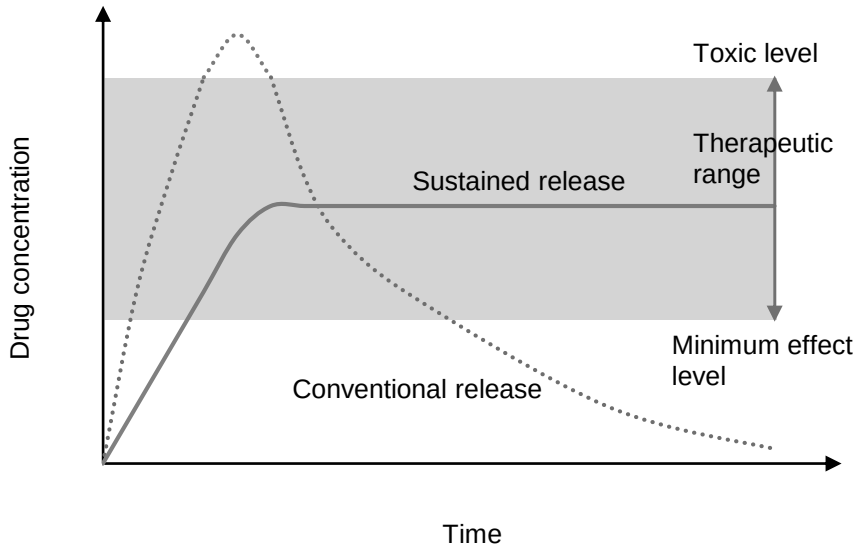


*Figure 1.2 Schematic of different drug release profiles*

There are different ways of coating pellets, and among them the Wurster coating process (Wurster, 1959) has proven to be highly efficient (Teunou & Poncelet, 2002). It is well known that the coating process that is used to produce the controlled release film affects the release of the drug substances and therefore the performance of the medicine. It is thus of great interest to study and understand the Wurster coating process in greater detail.

## 1.2. The Wurster coating process

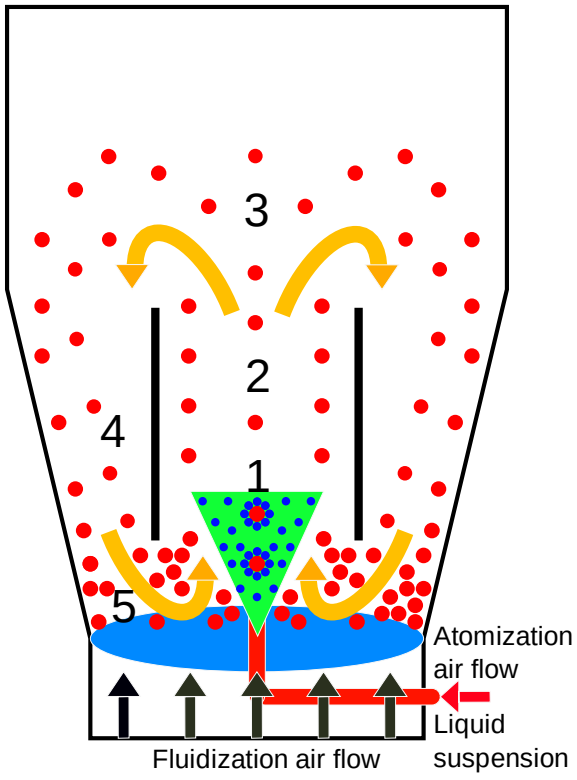


*Figure 1.3 Schematic of the Wurster process and the different regions: 1) the spray zone, 2) the Wurster tube, 3) the fountain region, 4) the downbed region, and 5) the horizontal transport region.*

The Wurster coating process is a bottom-spray coating process that takes place in a fluidized bed. At the bottom of the fluidized bed, a distributor plate with a

specific pattern of orifices determines the distribution of the hot fluidization airflow. This airflow is partly responsible for the motion of pellets. Also, there are one or more two-fluid spray nozzles at the bottom of the fluidized bed. These spray nozzles supply a liquid solution as well as an atomization airflow that breaks the solution into small droplets. The spray nozzles thus form a spray region at the bottom of the fluidized bed. As the pellets travel through this region, they receive a coating solution in the form of droplets, and, as they move around in the fluidized bed, the liquid droplets are dried by the hot airflow to form a film layer on each pellet.

Based on particle behavior, the fluidized bed can be divided into different regions, as sketched in Figure 1.3 (Christensen & Bertelsen, 1997; Karlsson *et al.*, 2011). During coating pellets receive the coating solution in the spray zone, and then dry as they return to the spray zone after having traveled through the Wurster tube, the downbed, and the horizontal transport regions. This sequence of coating and drying as the pellets travel through the different regions of the fluidized bed is referred to as a particle coating cycle (Li, Rasmuson*, et al.*, 2015).

The time it takes for a pellet to complete a cycle is defined as the cycle time. Similarly, the time that a pellet spends in a specific region is defined as the residence time in that region. Not only may a pellet behave differently from other pellets, but a pellet in one cycle can also behave differently from that same pellet in a different cycle. It is thus clear that pellets have both a cycle time distribution (CTD) and a residence time distribution (RTD) in different regions. The CTD and the RTD of particles in the spray zone together determine the amount of coating deposited on the pellets. Since the performance of the medicine to a great extent depends on the thickness of the coating film, it is clear that the CTD and the RTD of particles in the spray zone are critical factors in determining the coating film thickness and its variability (Mann & Crosby, 1975;

Cheng & Turton, 2000; Shelukar *et al.*, 2000; Turton, 2008). Furthermore, the drying rate, which is affected by the RTD of particles in different regions, is also expected to affect the quality of the coating film (Karlsson *et al.*, 2009) and, hence, the quality of the final product.

## 1.3. Objectives

Due to insufficient understanding of the underpinning mechanisms that affect the coating quality of individual pellets in a larger population, the aim of this study is to develop a mathematical model that is capable of predicting the fluidized bed coating process. This was carried out in several steps, as explained below.

The first step (Paper I (Li, Rasmuson*, et al.*, 2015)) was to gain a basic understanding of particle motion in the fluidized bed. In this step, the positron emission particle tracking (PEPT) technique was employed. A series of PEPT experiments were performed to investigate the movement of pellets and to determine the CTD and the RTD of particles in different regions. Several different geometrical configurations and operating parameters were considered. In particular, different size pellets were employed to identify the underpinning mechanisms by which the coating thickness changes.

In the second step (Paper II (Li, Remmelgas*, et al.*, 2015)), the characteristics of particle movement obtained, such as particle velocity, the CTD and the RTD of particles in different regions, were selected to evaluate the model for pellet motion based on the discrete element method, computational fluid dynamics (DEM-CFD) simulations. In an effort (Paper III (Li *et al.*, 2016)) to refine the sub-models in the DEM, the effect of the drag model, which determines the

interphase momentum transfer between the particles and the airflow, was investigated.

In a third step (Paper II), the detailed pellet motion in the spray zone was studied. A simple model for predicting the growth rate of pellets was developed based on the data available from the DEM-CFD simulations and the PEPT experiments. This predictive model was then evaluated by comparing coating experiments carried out under similar conditions (Paper IV).

In a final step, models for the wetting and drying of pellets were developed (Paper V). The calculated temperature and the amount of liquid in air can be compared to the measurement at selected locations. Then it can be possible to obtain the temperature and the amount of liquid for individual particles via DEM-CFD simulations. In addition, varying drying rates can be identified in different regions for an improved understanding of how the drying rate of particles in different regions affects the coating quality.

## 1.4. Outline of the thesis

The thesis is organized as follows. In the next chapter, the set-up of the systems used in this study is given to provide a basic understanding of the systems under investigation. Chapter 3 describes the modeling methods for both the movement and drying of pellets. In this chapter, assumptions and simplifications are discussed and the governing equations for the modeled phenomena are given in detail. Then the equipment, the materials, the operating conditions and the method of analysis used in the PEPT measurements and coating experiments are presented in Chapter 4. In Chapter 5, the main findings from the experimental and modeling work are discussed. Last, conclusions are drawn and an outlook is provided.

# 2. Set-up of the system

Prior to describing modeling methods and experiments, it is of interest to have a basic understanding of the systems that are used in this study.

## 2.1. STREA-1™

For the study of particle motion, the fluidized bed was based on the STREA-1™ laboratory fluidized bed from Aeromatic-Fielder. This experimental set-up was used for both the PEPT experiments and the DEM-CFD simulations of particle motion.

As shown in Figure 2.1 and Table 2.1 the total height of this fluidized bed was 380 mm, and the top and bottom diameters were 250 mm and 114 mm respectively. It was equipped with a bowl-shaped distributor with a diameter of 52 mm at the bottom of the bed. The center of this bowl-shaped distributor, i.e. the annular region between $D_b$ and $D_i$ in Figure 2.1, was fully open and covered the entire base. Outside this central region of the distributor, there was an annulus region, on which a number of orifices were distributed. These orifices in total took approximately 4% of the area of the annulus region of the distributor.

The atomization nozzle was located at the center towards the bottom of the fluidized bed. In this study, the nozzle was only a circular orifice with a diameter of 5 mm. No liquid solution was introduced. The diameter of the nozzle was much larger than a real atomization nozzle in order to reduce the numerical difficulties in simulating supersonic flow. In addition, a wire mesh screen was put over the distributor to prevent pellets from falling through the distributor.

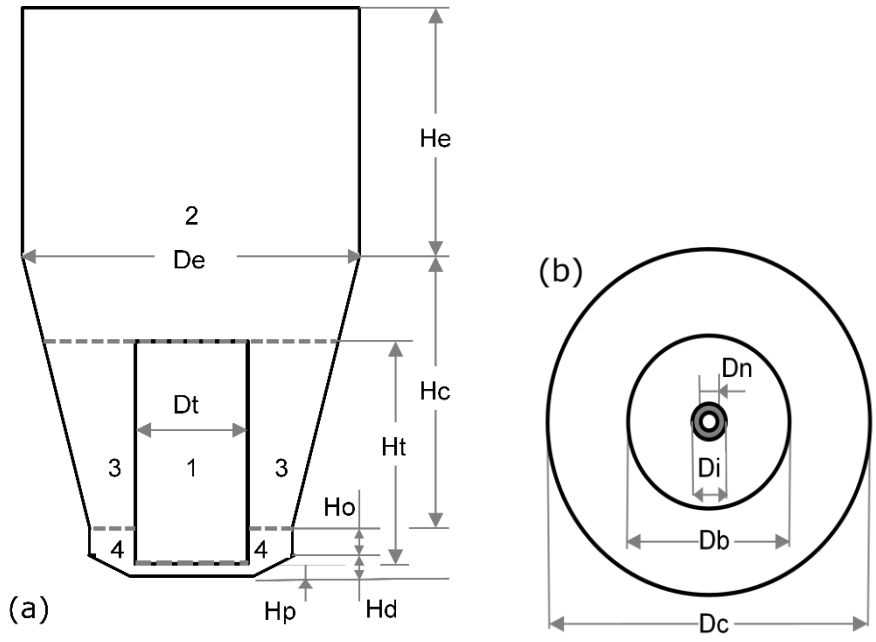


*Figure 2.1 The dimensions of the Wurster bed, a) side view showing the different regions: (1) the Wurster tube, (2) the fountain region, (3) the downbed region, and (4) the horizontal transport region; b) top view.*

*Table 2.1 The dimensions of the STREA-1 and LAB CC fluidized bed (in mm).*

| Variable | STREA-1 | LAB CC |
|---|---|---|
| Diameter of expansion chamber, $D_e$ | 250 | 250 |
| External diameter of the Wurster tube, $D_t$ | 50 | 50 |
| Upper diameter of bowl distributor plate, $D_c$ | 114 | 100 |
| External diameter of the base of bowl distributor plate, $D_b$ | 52 | - |
| Internal diameter of the base of bowl distributor plate, $D_i$ | 12 | 16 |
| Diameter of nozzle, $D_n$ | 5 | - |
| Height of expansion chamber, $H_e$ | 160 | 730 |
| Height of truncated cone, $H_c$ | 220 | 330 |
| Height of the Wurster tube, i.e., tube length, $H_t$ | 100, 150, 200 | 60 |
| Height of the connection between bowl distributor and truncated cone, $H_o$ | 20 | - |
| Height of bowl distributor, $H_d$ | 17 | - |
| Height of partition gap, $H_p$ | 10, 15, 20 | 20 |

## 2.2. LAB CC

For the coating and drying of pellets, the LAB CC system was employed. This system is commonly used for laboratory-scale coating experiments in pharmaceutical development. In this research, it was employed to perform coating and drying experiments in order to evaluate the predictive model for the growth of pellets and the drying model under development. In the experiments, an actual two-fluid spray nozzle was used.

This system consisted of a fluidized bed, an air supply system, a heater, sensors and user interfaces. The fluidized bed was 1060 mm high, with bottom and top diameters of 100 and 250 mm, respectively. Other dimensions are given in Table 2.1. It should be noted that a flat distributor was employed for the LAB CC fluidized bed (rather than the bowl-shaped distributor that was used for the STREA-1 fluidized bed).

# 3. Modeling methods

## 3.1. Overview of multiphase models

In modeling pellet motion in a fluidized bed, two basic approaches are available. These two approaches, usually referred to as Eulerian-Eulerian (EE) and Eulerian-Lagrangian (EL), are commonly used to model multiphase systems of gas and solid particles as in this study. They are briefly described in this section.

### 3.1.1. Eulerian-Eulerian approach

In the EE approach, both the gas phase and particle phase are treated as continuous, interpenetrating fluids. Since both phases are modeled as fluids, this approach is often also referred to as the two-fluid model (TFM). The governing equations are similar to those for single-phase flow, but a key quantity, the volume fraction for each phase, is introduced so that the relative amount of each phase can be determined at each location. Since only one set of conservation equations is employed for each phase, this approach is feasible regardless of the scale of systems. The EE approach is therefore frequently used for large-scale systems involving many particles. Inherently, this approach provides an averaged description of a multiphase system and requires additional relations for coupling.

### 3.1.2. Eulerian-Lagrangian approach

Unlike the EE approach, particles are in the EL approach tracked as an assembly of particles or as individual particles. In the former case, a number of particles that are followed simultaneously are treated as parcels. In the latter

case, which is the so-called discrete element method, the motion of every particle is considered.

In pharmaceutical development, laboratory-scale systems for pellet coating often contain a few gram to a few hundred gram almost spherical particles with a diameter that ranges from 200 to 1000 μm. This corresponds to tens of thousands to a few million particles, which can be simulated at a reasonable computational cost. Pilot-scale systems contain more particles and are more challenging to simulate. However, there is a steady increase in the computational power and simulations of 25 million particles have been reported recently by Jajcevic *et al.* (2013).

Thus, the DEM offers a unique opportunity to study pellet coating at the level of a single pellet. With the DEM, it is feasible and reasonably straightforward to account for different forces, including particle-particle and particle-wall collisions. In addition, it is possible in the DEM to implement a particle size distribution (PSD) and to study the variability in the pellet size that is usually encountered in practice, which is difficult to account for in the EE approach. These factors therefore motivate developing a DEM based model for pellet coating in a laboratory-scale fluidized bed and, in the future, to extend it to pilot-scale systems and eventually to industrial-scale systems.

## 3.2. Movement of pellets

In this section, the movement of pellets is described using the DEM. First, the mathematical model for the DEM based on a soft-sphere model is presented. Second, the governing equations for the gas flow are given. Last, the coupling between the particle phase and the gas phase is discussed.

### 3.2.1. Discrete element method

Basically, the DEM is based on Newton's second law of motion. The motion of every pellet is then written via a force balance:

$$m_{p,i}\frac{d\boldsymbol{v_{p,i}}}{dt} = \beta\frac{V_{p,i}}{\varepsilon_s}\left(\boldsymbol{u_g} - \boldsymbol{v_{p,i}}\right) + m_{p,i}\boldsymbol{g} - V_{p,i}\nabla P + \boldsymbol{F_{c,i}} \qquad (3.1)$$

where the terms on the RHS represent, in order, interphase momentum transfer, gravity, the force due to the pressure gradient, and the contact force due to particle-particle and particle-wall collisions. In this equation, $m_{p,i}$ is the mass of the $i^{th}$ pellet, $\boldsymbol{v}_{p,i}$ is the velocity of the $i^{th}$ pellet, $\boldsymbol{u}_g$ is the velocity of the air, $\boldsymbol{g}$ is the gravitational acceleration, $V_{p,i}$ is the volume of the $i^{th}$ pellet, $\nabla P$ is the gradient of the air pressure, $\varepsilon_s$ is the particle/solid volume fraction, and $\beta$ is the interphase momentum transfer coefficient.

The angular momentum of the pellet is calculated by

$$I_{p,i}\frac{d\boldsymbol{\omega_{p,i}}}{dt} = \sum \boldsymbol{T}_{p,i} \qquad (3.2)$$

where $I_{p,i}$ is the moment of inertia, $\boldsymbol{\omega}_{p,i}$ is the rotational velocity, and $\boldsymbol{T_{p,i}}$ is the total torque acting on the particle.

For the contact force due to particle-particle and particle-wall collisions, it is well-known that there are two models available: the hard sphere and soft sphere models. In the hard sphere model, the interaction forces are assumed to be impulsive and all other forces are negligible during collisions (Crowe *et al.*, 2012). The hard sphere model is easy to use but limited to only binary collisions. In the soft sphere model, the deformation of particles in contact is modeled in a straightforward fashion using the Hertz-Mindlin theory (Hertz, 1882); the local linear deformation is related to the normal and tangential forces respectively.

The soft sphere model implements the physics of collisions more directly but at a higher computational cost. In this study, since pellets can remain in contact for a long time in the dense region of the fluidized bed, the soft sphere model has been used, as described below.

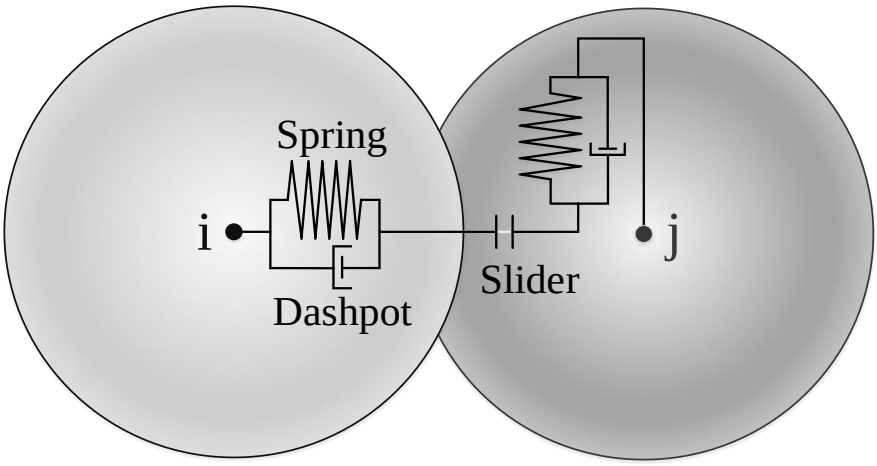


*Figure 3.1 A schematic of the soft sphere model*

When particles collide with each other, their deformation is modeled via an overlap between them and the energy loss during the collision is accounted for through a so-called spring-dashpot system, as illustrated in Figure 3.1. This system is characterized using the spring stiffness, $k$, the damping coefficient, $\eta$, and the friction coefficient, $\mu_p$. The latter quantity ($\mu_p$) is empirical and can be measured by e.g. using a Jenike shear cell (Jenike, 1961; Darelius *et al.*, 2007). The former two quantities can be calculated according to the Hertz-Mindlin theory (Hertz, 1882; Dintwa *et al.*, 2007), as explained below.

The normal and tangential contact forces acting on the particle, $\boldsymbol{F_{cn,ij}}$ and $\boldsymbol{F_{ct,ij}}$, are given by (Crowe *et al.*, 2012)

$$\boldsymbol{F_{cn,ij}} = -\left(k_n \delta_n^{3/2} \boldsymbol{n}_{ij} - \eta_{nj} \boldsymbol{v}_{ij} \cdot \boldsymbol{n}_{ij}\right) \boldsymbol{n}_{ij} \tag{3.3}$$

$$\boldsymbol{F}_{ct,ij} = \begin{cases} -k_t \boldsymbol{\delta}_t - \eta_{tj} \boldsymbol{v}_{ct} & if \quad \left|\boldsymbol{F}_{ct,ij}\right| \leq \mu_p \left|\boldsymbol{F}_{cn,ij}\right| \\ -\mu_p \left|\boldsymbol{F}_{cn,ij}\right| \boldsymbol{t}_{ij} & if \quad \left|\boldsymbol{F}_{ct,ij}\right| > \mu_p \left|\boldsymbol{F}_{cn,ij}\right| \end{cases} \tag{3.4}$$

where $\delta$ represents the displacement of the particle caused by the normal or tangential force, $\boldsymbol{n}_{ij}$ and $\boldsymbol{t}_{ij}$ are the unit vectors normal and tangential to the contact plane, respectively, $\boldsymbol{v}_{ij}$ is the relative velocity between particle $i$ and particle $j$, and $\boldsymbol{v}_{ct}$ is the slip velocity of the contact point. The suffixes $n$ and $t$ denote the components in the normal and tangential directions, while the suffixes $i$ and $j$ denote particle $i$ and particle $j$, respectively.

The normal and tangential stiffnesses, $k_n$ and $k_t$, are expressed by

$$k_n = \frac{4}{3}\left(\frac{1-\sigma_i^2}{E_i} + \frac{1-\sigma_j^2}{E_j}\right)^{-1}\left(\frac{r_i + r_j}{r_i r_j}\right)^{-1/2} \tag{3.5}$$

$$k_t = 8\left(\frac{1-\sigma_i^2}{H_i} + \frac{1-\sigma_j^2}{H_j}\right)^{-1}\left(\frac{r_i + r_j}{r_i r_j}\right)^{-1/2}\delta_n^{1/2} \tag{3.6}$$

where $E$ is the Young's modulus, $\sigma$ is the Poisson's ratio, $H = \frac{E}{2(1+\sigma)}$ is the shear modulus and $r$ is the radius of the particle.

In Eq. (3.3) and Eq. (3.4), the damping coefficient $\eta$, which represents the viscous dissipation of kinetic energy in the normal and tangential directions, can be obtained according to Tsuji *et al.* (1992); (1993),

$$\eta_n = 2\alpha\sqrt{m_p{}^* k_n}\delta_n^{1/4} \tag{3.7}$$

$$\eta_t = 2\alpha\sqrt{m_p{}^* k_t} \tag{3.8}$$

where $\alpha$ denotes a constant related to the coefficient of restitution, which is given in the work of Tsuji *et al.* (1992), and $m_p{}^*$ represents the effective particle mass and is calculated by

$$m_p{}^* = \frac{m_{p,i} m_{p,j}}{m_{p,i} + m_{p,j}} \tag{3.9}$$

A more detailed description of the model can be found in the literature (Cundall & Strack, 1979; Tsuji *et al.*, 1993; Deen *et al.*, 2007; Crowe *et al.*, 2012).

### 3.2.2. Gas flow

As mentioned earlier, there is an atomization airflow with a high velocity at the bottom of the fluidized bed. From the atomization airflow rate and the diameter of the nozzle, the Reynolds number is estimated to be approximately $10^4$. For single-phase airflow with such high Reynolds number, turbulence may therefore be expected. Nevertheless, since the Stokes number of the large particles in this study is quite large, St>>1, it may be assumed that turbulence near the nozzle will not have an appreciable effect on particle trajectories. Additionally, for dense gas-solid flows, such as the one included in this study, the particle stress is expected to be much greater than the stress due to turbulence (Hrenya & Sinclair, 1997). Turbulence is therefore neglected.

Therefore, the continuity and momentum equations for the airflow can be written:

$$\frac{\partial}{\partial t}\left(\varepsilon_g \rho_g\right) + \nabla \cdot \left(\varepsilon_g \rho_g \boldsymbol{u}_g\right) = 0 \tag{3.10}$$

$$\frac{\partial}{\partial t}\left(\varepsilon_g \rho_g \boldsymbol{u}_g\right) + \nabla \cdot \left(\varepsilon_g \rho_g \boldsymbol{u}_g \boldsymbol{u}_g\right) = -\varepsilon_g \nabla P - \nabla \cdot \left(\varepsilon_g \boldsymbol{\tau}_g\right) + \varepsilon_g \rho_g \boldsymbol{g} - \sum_{i=1}^{n} \beta\left(\boldsymbol{u}_g - \boldsymbol{v}_{p,i}\right) \tag{3.11}$$

where $\varepsilon_g = 1 - \varepsilon_s$ is the gas volume fraction, $\rho_g$ is the density of the air, $\mu_g$ is the dynamic viscosity of the air, $d_p$ is the particle diameter and $\boldsymbol{\tau_g}$ is the viscous stress tensor for incompressible flow,

$$\boldsymbol{\tau}_g = \mu_g \left(\nabla \boldsymbol{u}_g + \left(\nabla \boldsymbol{u}_g\right)^T\right) \tag{3.12}$$

### 3.2.3. Drag model

The momentum transfer between the particles and the air is given by the interphase momentum transfer term as given in Eqs. (3.1) and (3.11), which is

determined by the interphase momentum transfer coefficient, $\beta$. This interphase momentum transfer coefficient can be specified using different drag models. This study mainly relies on the Gidaspow drag model (Gidaspow, 1994), but also explores four other models for the possibility of refinement: the Min, HKL, Beetstra and Tang drag models. The latter three models are based on simulations of flow through assemblies of particles using the Lattice-Boltzmann method (LBM) or the immersed boundary method (IBM) while the Min drag model is merely the minimum of the Ergun and Wen-Yu drag models. These drag models give different interphase momentum transfer coefficients, as shown in Figure 3.2, for varying relative velocities and volume fractions. Details about the Gidaspow drag model are given below, while details about the other four drag models can be found in Paper III.

The Gidaspow drag model is based on the Ergun equation (Ergun, 1952) for the dense regime and the Wen and Yu correlation (Wen & Yu, 1966) for the dilute regime,

$$\beta_{Gidaspow} = \begin{cases} \beta_{Ergun} = \left(150\frac{{\varepsilon_s}^2}{\varepsilon_g} + 1.75\varepsilon_s Re_p\right)\frac{\mu_g}{{d_p}^2} & \varepsilon_s > 0.2 \\ \beta_{Wen-Yu} = \frac{3}{4}Re_p C_D \frac{\mu_g \varepsilon_s}{{d_p}^2}{\varepsilon_g}^{-2.65} & \varepsilon_s \leq 0.2 \end{cases} \tag{3.13}$$

where $C_D$ is the drag coefficient, which is written as

$$C_D = \begin{cases} 24\left(\frac{1 + 0.15{Re_p}^{0.687}}{Re_p}\right) & Re_p < 1000 \\ 0.44 & Re_p \geq 1000 \end{cases} \tag{3.14}$$

and $Re_p$ is the particle Reynolds number,

$$Re_p = \varepsilon_g \rho_g \left|\boldsymbol{u}_g - \boldsymbol{v}_{p,i}\right| \frac{d_p}{\mu_g} \tag{3.15}$$

This drag model was found to be the best for modeling spouted beds (Du *et al.*, 2006) and has been widely used in engineering practice (Deen *et al.*, 2007).

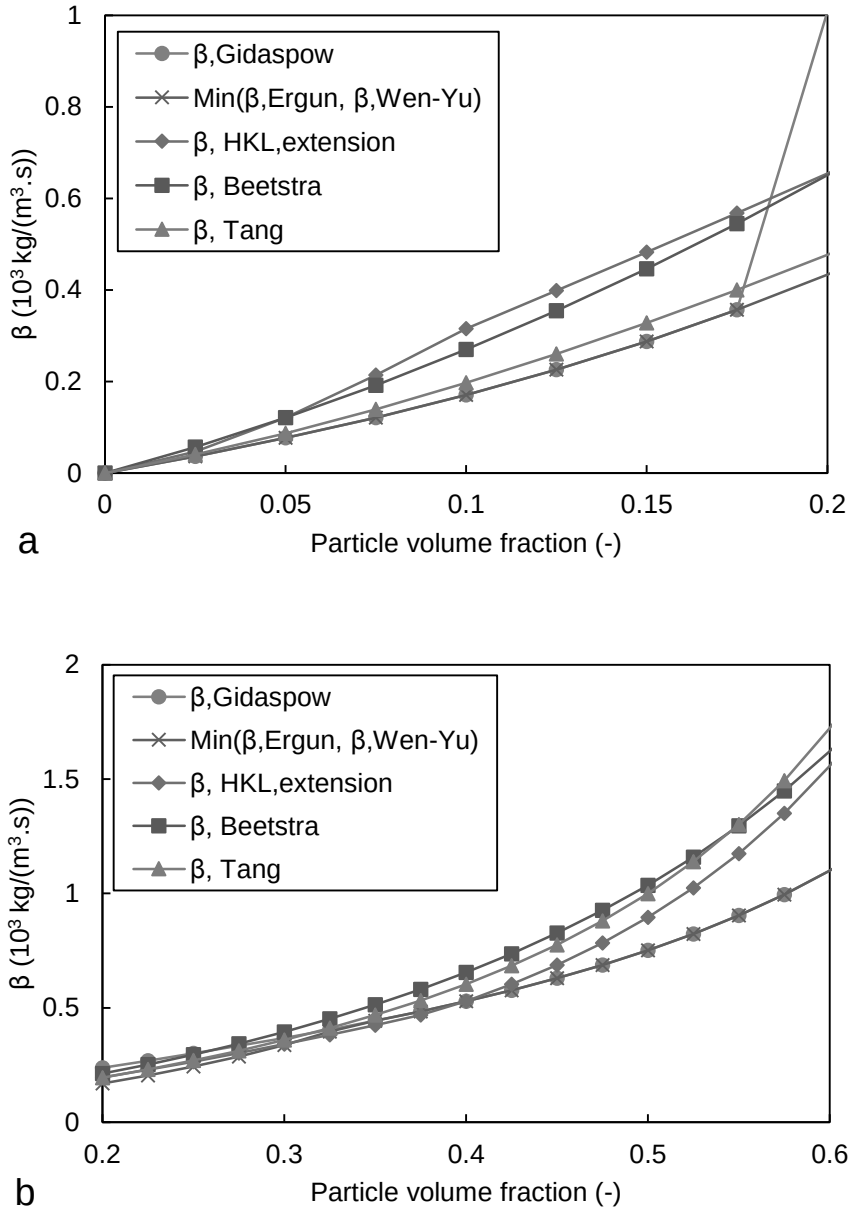


*Figure 3.2 Comparison of drag models, the relative velocity between gas flow and particles is (a) 5 m/s and (b) 1 m/s, respectively.*

## 3.3. Numerical methods

To solve the governing equations presented above, a fully-coupled multiphase solver, MultiFlow (http://www.multiflow.org), developed by van Wachem's research group, was employed. In MultiFlow, the continuous phase is predicted using the finite volume method (FVM) via the Rhie and Chow (1983) interpolation for pressure and velocity coupling. For spatial discretization, the second-order central difference scheme is used for non-convective terms while the second-order upwind scheme is used for convective terms. The time discretization is based on the second-order backward scheme (Jorn Bruchmüller, 2011).

It is worth mentioning that a multigrid technique was employed in this research to couple the discrete and continuous phases as described by e.g. J. Bruchmüller *et al.* (2010); (2011). With this technique, the continuous phase is solved on a hexahedral mesh while particles are tracked on a so-called particle mesh, which is a Cartesian mesh with a mesh size that is larger than the particle. All the coupling terms, including the volume fraction and the drag force, are determined on the length-scale of this particle mesh. In particular, if the local fluid cell is smaller than a particle, the coupling between that fluid cell and the particle occupying that fluid cell is length-scale weighted, and therefore remain physical. This way of addressing the very large volume fraction present in dense particle flow has been described and tested by Mallouppas and van Wachem (2013), and has been further worked out in the recent work of Capecelatro and Desjardins (2013).

In terms of boundary conditions, a velocity inlet normal to the boundary was applied at the distributor and at the spray nozzle. At the outlet of the fluidized bed, a pressure outlet was employed. In addition, the walls of the fluidized bed

and the Wurster tube, which are treated as adiabatic, were set to be no-slip for the continuous phase.

## 3.4. Drying of pellets

As mentioned earlier, for a given polymer film, the coating quality not only depends on the film thickness but can also depends on the drying rate of the liquid film. In this study, it is assumed that as a pellet passes through the spray zone and receives the coating solution, an evenly spread liquid film is formed quickly around the surface of the pellet. As the pellet leaves the spray zone, it is dried by the hot airflow as described as follows.

**Mass conservation of liquid in pellets:**

$$\frac{\partial m_{p,w}}{\partial t} = A_p N_{w,p} \tag{3.16}$$

where $A_\mathrm{p}$ is the surface area of the pellet, $N_{w,p}$ is the mass flux of liquid through the surface of the pellet, $m_{p,w}$ is the mass of the pellet. Here the total mass of the pellet is the sum of the mass of the solid core, $m_p$, the mass of the solvent, $m_w$, and the mass of the polymer substance, $m_{sub}$:

$$m_{p,w} = m_p + m_w + m_{sub} \tag{3.17}$$

Eq. (3.16) can then be written as

$$\frac{\partial m_w}{\partial t} = A_p N_{w,p} \tag{3.18}$$

For simplification, the following assumptions are made in a first model attempt:

i. In the first drying stage, the pellet surface is saturated with liquid;

ii. In the intermediate drying stage, the drying rate falls mainly due to the decreased vapor pressure at equilibrium. In reality, the drying rate can also decrease due to an increase in the mass transfer resistance, but this effect is not taken into account.

iii. The change in the film thickness does not affect the hydrodynamics of pellet motion.

The mass flux of liquid to the surface of the pellet during drying can be written as

$$N_{w,p} = \frac{k_{pg} M_w}{R}\left(\frac{P_{w,p}}{T_p} - \frac{P_{w,g}}{T_g}\right) \qquad (3.19)$$

In Eq. (3.19), $k_{pg}$ is the mass transfer coefficient, $M_w$ is the molar weight of the solvent, $R$ is the gas constant, $T_p$ and $T_g$ are the temperature of the pellet and the temperature of the air, respectively, $P_{w,g}$ is the partial pressure of the solvent in air and $P_{w,p}$ is the partial pressure of the solvent over the surface of the pellet.

In the first stage, $P_{w,p}$ can be calculated according to the Antoine equation for the saturated vapor of the solvent, $P_{w,sat}$,

$$P_{w,p} = P_{w,sat} = \frac{101325}{760} 10^{\left(A - \frac{B}{T_p - 273.15 + C}\right)} \qquad (3.20)$$

where $A, B$ and $C$ are constants for the specified solvent, such as water in this study. In Eq. (3.20), the units for pressure and temperature are Pascal and Kelvin, respectively.

In the second stage, the decrease in driving force caused by the lower vapor pressure at equilibrium with the polymer film is accounted for. In this case, the partial pressure of the solvent over the surface of the pellet can be related to the saturated vapor of the solvent,

$$P_{w,p} = f(X) * P_{w,sat} \tag{3.21}$$

where $f(X)$ is a function of the mass fraction of the solvent in the pellet, $Y_{w,p}$,

$$f(X) = 100(1 - exp(-k\, {Y_{w,p}}^N)) \tag{3.22}$$

where $k$ and $N$ are constants that can be determined by fitting the experimental data for the specified material. In Eq. (3.22), $Y_{w,p}$ can also be related to the mass fraction of the solvent in the coating film, for example, as shown in Figure 3.3.

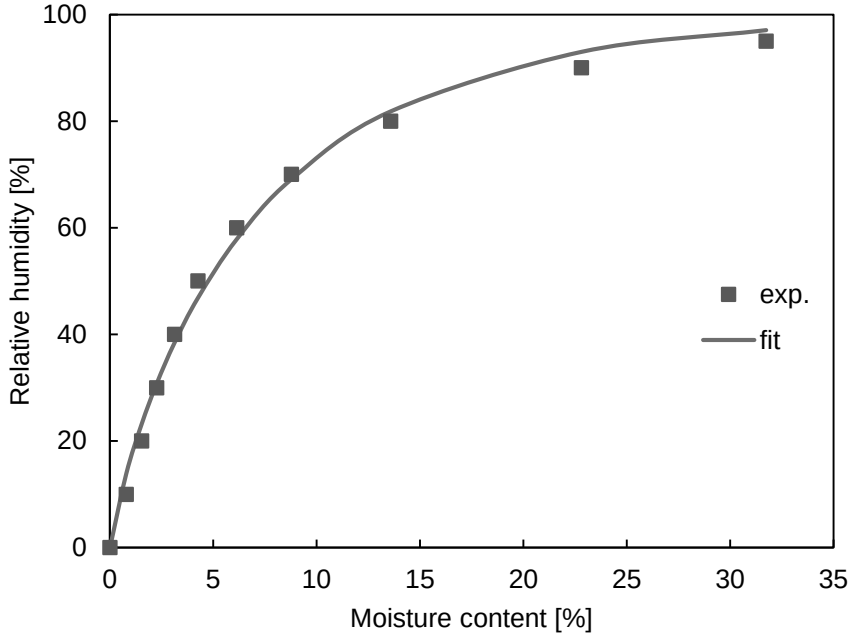


*Figure 3.3 The relation between relative humidity and moisture content, e.g. for HPMC.*

In Eq. (3.19), the correlations proposed by Gunn (1978) are used to calculate the mass transfer coefficient:

$$k_{pg} = \frac{D_{AB} Sh_p}{d_p} \tag{3.23}$$

$$Sh_p = \left(7 - 10\varepsilon_g + 5{\varepsilon_g}^2\right)\left(1 + 0.7 Re_p^{0.2} Sc^{1/3}\right) + \left(1.33 - 2.4\varepsilon_g + 1.2{\varepsilon_g}^2\right) Re_p^{0.7} Sc^{1/3} \tag{3.24}$$

$$Sc = \frac{\mu_g}{\rho_g D_{AB}} \tag{3.25}$$

where $Sh_p$ is the Sherwood number of the pellet, $Sc$ is the Schmidt number of the air, $D_{AB}$ is the diffusivity of the solvent in air.

Then the mass fraction of the solvent, $Y_{w,p}$, can be related to the film thickness, $l_{film}$:

$$Y_{w,p} = \frac{m_w}{m_p} = \frac{A_p l_{film} \phi_1 \rho_w}{m_p} \tag{3.26}$$

where $m_w$ is the mass of the solvent, $\phi_1$ is the volume fraction of the solvent and $\rho_w$ is the density of the solvent.

**Energy equation over pellets:**

$$m_p c_{p,p} \frac{\partial T_p}{\partial t} = -h_{pg} A_p \left(T_p - \widetilde{T_f}\right) - H_{evap} S_{w,p} \tag{3.27}$$

where the first and second terms on the RHS represent the convective heat transfer and the heat transfer due to evaporation of the solvent. In Eq. (3.27), $c_{p,p}$ is the specific heat capacity of the pellet, $h_{pg}$ is the convective heat transfer coefficient estimated from the Nusselt number, which has a form similar to Eq. (3.23), $\widetilde{T_f}$ is the interpolated fluid temperature as seen by the pellet, $H_{evp}$ is the latent heat of evaporation and $S_{w,p} = \frac{\partial m_w}{\partial t}$ is the evaporation rate.

**Mass conservation of solvent for the fluid phase:**

$$\frac{\partial \varepsilon_g \rho_g Y_{w,g}}{\partial t} + \nabla \cdot \left(\varepsilon_g \rho_g \boldsymbol{u_g} Y_{w,g}\right) = \nabla \cdot \left(\varepsilon_g D_{AB} \nabla Y_{w,g}\right) - S_{w,g} \tag{3.28}$$

where $Y_{w,g}$ is the mass fraction of the solvent in air. Here, $S_{w,g}$ is the solvent exchange rate between the air and the particles:

$$S_{w,g} = -\sum S_{w,p} \tag{3.29}$$

**Energy equation for the fluid phase:**

$$\frac{\partial \varepsilon_g \rho_g c_{p,g} T_g}{\partial t} + \nabla \cdot \left(\varepsilon_g \rho_g \boldsymbol{u_g} c_{p,g} T_g\right) = \nabla \cdot \left(\varepsilon_g \lambda_g \nabla T_g\right) + Q_{pg} + H_{evap} S_{w,g} \qquad (3.30)$$

where $c_{p,g}$ is the heat capacity of the air and $\lambda_g$ is the thermal conductivity of the air.

In Eq. (3.30), $Q_{pg}$ is the heat exchange rate between the air and the particles:

$$Q_g = \sum \frac{6\varepsilon_g h_{pg}\left(T_p - T_g\right)}{d_p} \qquad (3.31)$$

# 4. Experimental

## 4.1. PEPT

### 4.1.1. The PEPT measurement system

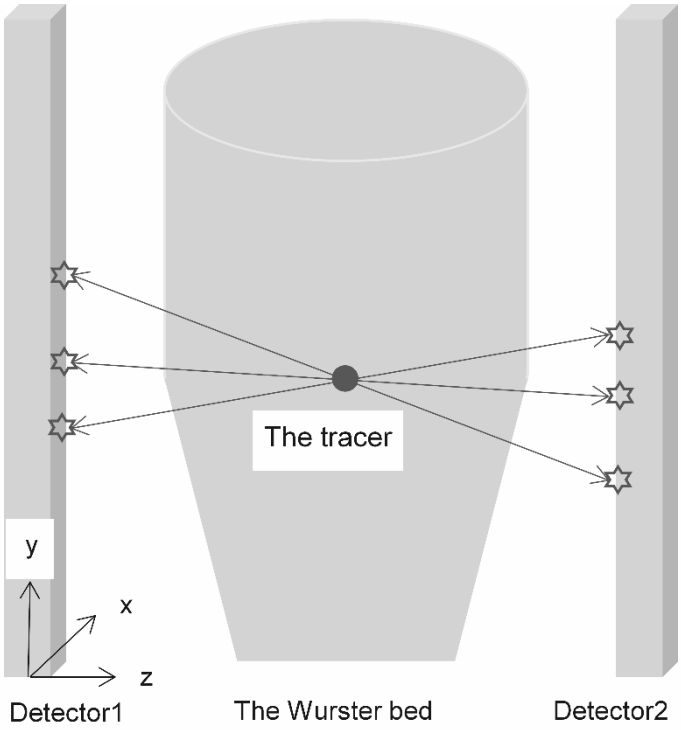


*Figure 4.1 Schematic of the PEPT measurement system*

As illustrated in Figure 4.1, the PEPT measurement system consisted of a fluidized bed (containing particles) in the middle, two position-sensitive detectors on both sides of the fluidized bed and a tracer particle. The tracer particle was marked with a radioactive isotope that releases $\gamma$-rays. As the tracer particle moves around in the equipment, the $\gamma$-rays are captured by the detectors. Then it is possible to define a line of response (LOR) along which the tracer particle lies by following the pair of $\gamma$-rays detected simultaneously. After a sufficient number of pairs of $\gamma$-rays have been obtained, the location of the tracer particle in three dimensions can be found through geometric triangulation. More details about the

technique and the algorithm have been presented elsewhere by Parker *et al.* (1993); (1997; 2002).

### 4.1.2. Materials

In this study, microcrystalline cellulose (MCC) pellets, which are commonly-used solid cores in the pharmaceutical industry, were employed. These MCC pellets, manufactured upon request by Umang Pharmatech Pvt. Ltd, are relatively large in order to limit the number of particles in the DEM-CFD simulations. The pellets were classified into two main groups according to their size distribution and the corresponding volume mean diameter (VMD): small (approximately 1.8 mm) and large (approximately 2.6 mm).

### 4.1.3. The tracer particle

Prior to the experiments, using a scanning electron microscope (SEM), a number of pellets with a diameter close to the VMD were selected from the respective small and large pellets for later labeling use. In each run, only one tracer particle was incorporated. This tracer particle was put in radioactive water for about half an hour so as to gain free 18F- via absorption and adsorption. Since the radioactivity lasts for about 6 hours, the same tracer particle could be used for several runs. Since the activity of the tracer particle decreases as a function of time, it was necessary to move the detectors closer to the fluidized bed in later runs.

### 4.1.4. Operating parameters

In the PEPT experiments, a suitable airflow rate was selected based on several preliminary tests. The objective of these tests was to find a flow rate that gave a desired representative of the pellet motion in a Wurster fluidized bed, as

described in the introduction. For a typical run, 200 g monosized small pellets were employed, while for mixtures, 25%, 50% and 75%, the 200 g particles were replaced with the large ones. In the preliminary tests, it was also found that a run time of 1.5 hours was sufficient to obtain a compromise between the quality of the data and the run time. A summary of the configurations and operating parameters can be found in Table 4.1 for each run. Run #2 was selected as the base case because its operating parameters were set to the middle level.

*Table 4.1 The configuration and operating parameters for each PEPT run.*

| Run # | Partition gap (mm) | Batch size (g) | Tube length (mm) | Mass of 1749 μm particles (g) | Mass of 2665 μm particles (g) | VMD of tracer particle (μm) | Fluidization airflow rate ($m^3/h$) | Atomization airflow rate ($m^3/h$) | Run time (h) |
|---|---|---|---|---|---|---|---|---|---|
| 1 | 10 | 200 | 150 | 200 | - | 1749 | 73.3 | 3.50 | 3 |
| 2 | 15 | 200 | 150 | 200 | - | 1749 | 73.3 | 3.50 | 1.5 |
| 3 | 20 | 200 | 150 | 200 | - | 1749 | 73.3 | 3.50 | 1.5 |
| 4 | 15 | 400 | 150 | 400 | - | 1749 | 73.3 | 3.50 | 1.5 |
| 5 | 15 | 600 | 150 | 600 | - | 1749 | 73.3 | 3.50 | 1.5 |
| 6 | 15 | 200 | 100 | 200 | - | 1749 | 73.3 | 3.50 | 1.5 |
| 7 | 15 | 200 | 200 | 200 | - | 1749 | 73.3 | 3.50 | 1.5 |
| 8 | 15 | 200 | 150 | - | 200 | 2665 | 80.3 | 4.32 | 1.5 |
| 9 | 15 | 200 | 150 | 150 | 50 | 1749 | 80.3 | 4.32 | 1.5 |
| 10 | 15 | 200 | 150 | 150 | 50 | 2665 | 80.3 | 4.32 | 1.5 |
| 11 | 15 | 200 | 150 | 100 | 100 | 1749 | 80.3 | 4.32 | 1.5 |
| 12 | 15 | 200 | 150 | 100 | 100 | 2665 | 80.3 | 4.32 | 1.5 |
| 13 | 15 | 200 | 150 | 50 | 150 | 1749 | 80.3 | 4.32 | 1.5 |
| 14 | 15 | 200 | 150 | 50 | 150 | 2665 | 80.3 | 4.32 | 1.5 |
| 15 | 15 | 200 | 150 | 200 | - | 1749 | 65.8 | 3.50 | 1 |
| 16 | 15 | 200 | 150 | 200 | - | 1749 | 80.3 | 3.50 | 1 |
| 17 | 15 | 200 | 150 | 200 | - | 1749 | 73.3 | 2.49 | 1 |
| 18 | 15 | 200 | 150 | 200 | - | 1749 | 73.3 | 4.54 | 1 |

### 4.1.5. Post-processing

In the PEPT experiments, the location of the tracer particle was obtained using the program, TRACK, which was developed by Parker *et al.* (1993). In the

algorithm used by the program, the events recorded by the PEPT cameras are divided into subsets of sequential events by specifying the number of events per slice, *#events/slice*. The location that minimizes the distance to the reconstructed paths is then calculated for each subset. As a next step, the events farthest from the calculated location are regarded as corrupted and are discarded. This procedure of discarding corrupted events is repeated until a certain fraction of the sequential events for each subset, $f_{opt}$, remain, at which point the location of the tracer particle is found. Then it is possible to calculate the average distance of all the LORs used to determine the location of the tracer particle from the calculated location. This average distance, i.e. *error*, then provides a measure of precision or reliability of that calculated location (Seville, 2010).

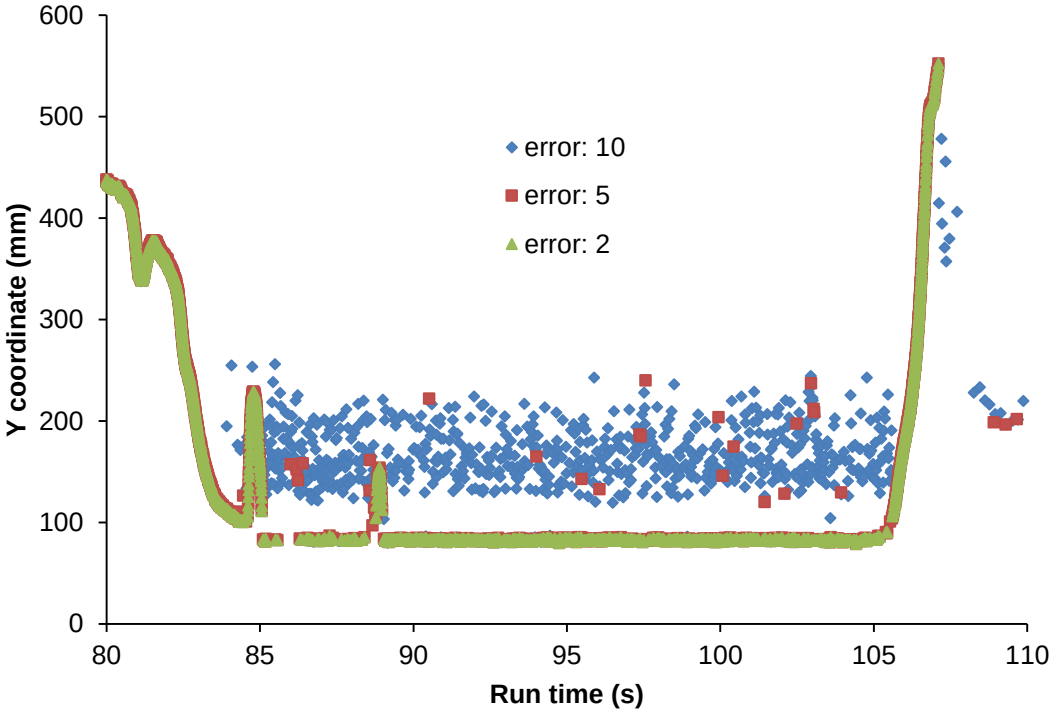


*Figure 4.2 An example showing the axial (y) coordinates of the tracer particle positioned on top of the nozzle with varying errors.*

The optimal values of these parameters depend on the particular geometries and flow conditions (Chiti, 2008). For the data obtained here, an example of the

removal of outliers with a varying error can be seen in Figure 4.2. Figure 4.2 shows that an error of 2 removes most of the outliers, but that it also greatly reduces the number of data points available. Thus, there is a trade-off between the accuracy or error and the number of data points obtained. High values for the number of events per slice, $f_{opt}$ and the error give a higher time resolution (i.e. more data points) but a lower reliability. On the other hand, low values of the number of events per slice, $f_{opt}$, and the error give a lower time resolution but a higher reliability. After a number of tests, values for the number of events per slice, $f_{opt}$ and the error that gave a sufficient time resolution and reliability were determined to be 500, 0.05 and 5, respectively. Using these parameter values, the sampling interval in this study remained in the range of 50-80 ms. In this range, the effect of these parameter values on e.g. the cycle time is relatively minor, as shown in Figure 4.3.

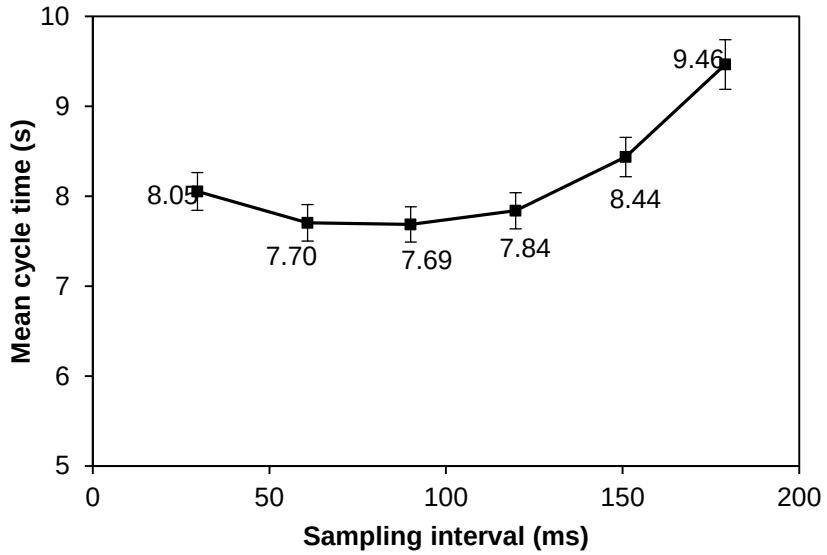


*Figure 4.3 The effect of the mean sampling interval on the mean cycle time (partition gap 10 mm, batch size 200 g, particle VMD 1749 µm, tube length 150 mm, fluidization airflow rate 73.3 m³/h, and atomization airflow rate 3.50 m³/h).*

## 4.2. Coating experiments

### 4.2.1. Materials

The pellets used in the coating experiments were the same as those used in the PEPT experiments. These pellets were mixed so as to produce the same total amount of mixtures with different fractions of large particles: 25%, 50% and 75%. A detailed composition of each mixture and the VMD of small and large pellets in each mixture are presented in Table 4.2.

*Table 4.2 Specification of uncoated small and large particles for different mixtures.*

| **Fraction of the large particles in each mixture (%)** | **Mass of the small particles (g)** | **Mass of the large particles (g)** | **Class of particles (-)** | **VMD (μm)** |
|---|---|---|---|---|
| **25** | 135 | 45 | Small | 1783 |
| | | | Large | 2704 |
| **50** | 90 | 90 | Small | 1768 |
| | | | Large | 2694 |
| **75** | 45 | 135 | Small | 1780 |
| | | | Large | 2675 |

### 4.2.2. QicPic analysis

In order to monitor the change in size of uncoated and coated pellets, an image analyzer, namely QicPic, was employed. With QicPic, both the size and shape of particles can be measured. In this measurement, the diameter of a pellet is defined as the diameter of a circle that has the same area as the projection area of the pellet. The sphericity is specified as the ratio of the perimeter of the equivalent circle to the real perimeter. In order to be able to collect the pellets after the measurement, the GRADIS dispenser was employed to ensure that the measurement was non-destructive.

### 4.2.3. Coating solution

The pellets were coated with a polymer solution containing ethyl cellulose (EC) and water-soluble hydroxypropyl cellulose (HPC). The coating solution was prepared by dissolving EC/HPC in ethanol at room temperature followed by stirring overnight. In this study, the EC/HPC polymer blend ratio was 50:50 w/w and the polymer concentration was 6% w/w.

### 4.2.4. Determination of growth of pellets

In this study, the size range of small and large pellets had an overlap to some extent. Since this overlap may cause difficulty in calculating the respective growth of small and large pellets, i.e. in determining whether a pellet is small or large, it was necessary to minimize the overlap. Therefore, screens with apertures of 2 mm and 2.5 mm were employed to sieve the pellets larger than 2 mm from the small pellets and the pellets smaller than 2.5 mm from the large pellets, respectively. Then mixtures of small and large pellets were prepared according to the specifications in Table 4.2. Since the small and large pellets have their own size distribution, the small and large pellets for each mixture were measured separately before mixing. Afterwards, the overall PSD of each mixture was measured.

After coating, it was found that the PSD of the mixtures depended very strongly on the sample size. Since it was impractical to measure all particles at the same time, each mixture was measured by splitting it into three parts and then calculating the overall PSD using a mass weighted average. In order to evaluate the growth of pellets after coating, a threshold particle size was selected to distinguish the small and large particles in each mixture. The threshold particle size for each mixture was specified as the particle size between 2000 and 2500 μm for which the weight fraction was the smallest.

## 4.3. Drying experiments

### 4.3.1. Method

In the drying experiments, the built-in sensors in the LAB CC system read the temperature and the humidity at the inlet and the outlet of the fluidized bed. In addition, six sensors, namely PyroButton®, are used to log the local humidity and the temperature. The PyroButton® has recently been utilized in pharmaceutical industry to improve understanding and assist process operation (Kona *et al.*, 2013; Pandey & Bindra, 2013). In this study, these sensors were employed to record the relative humidity (RH) and the temperature at selected locations in the Wurster tube.

### 4.3.2. Coating solution

In the drying experiments, the polymer solution with a polymer concentration of 6% was produced by dissolving and stirring HPMC in water for 24 hours. For each experiment, 20% weight increase to the core pellets was planned, which resulted in a consumption of approximately 730 g coating solution.

### 4.3.3. Operating parameters

In the drying experiments, small and large microcrystalline cellulose (MCC) pellets with diameters of 1.8 and 2.6 mm were employed. Operating parameters, i.e. fluidization airflow rate, air temperature and spray rate, were varied and summarized in Table 4.3. The fluidization and atomization air was dry. It is of interest to note that due to practical reasons, the highest spray rate was limited to approximately 18 g/min. Every run took approximately 40 minutes for coating and 2 minutes for additional drying after the coating solution was stopped. Since the PyroButtons® also receive an amount of coating solution, they were cleaned between runs. In addition, pure water was used in Run #8 to provide a reference.

*Table 4.3 The operating parameters used in the drying experiments.*

<table>
<tr><th>Run #</th><th>Mass of 1.8 mm pellets (g)</th><th>Mass of 2.6 mm pellets (g)</th><th>Fluidization airflow rate (m³/h)</th><th>Atomization airflow rate (m³/h)</th><th>Air temperature (°C)</th><th>Spray rate (g/min)</th></tr>
<tr><td>1</td><td>-</td><td>175</td><td rowspan="2">60</td><td rowspan="8">2.5</td><td rowspan="3">75</td><td rowspan="5">18</td></tr>
<tr><td>2</td><td>175</td><td>-</td></tr>
<tr><td>3</td><td rowspan="4">-</td><td rowspan="4">175</td><td>50</td></tr>
<tr><td>4</td><td>70</td></tr>
<tr><td>5</td><td rowspan="3">60</td><td>60</td></tr>
<tr><td>6</td><td>90</td></tr>
<tr><td>7</td><td rowspan="2">175</td><td rowspan="2">-</td><td rowspan="2">75</td><td>10</td></tr>
<tr><td>8</td><td>18</td></tr>
</table>

# 5. Results and discussion

## 5.1. Characteristics of particle motion (Paper I)

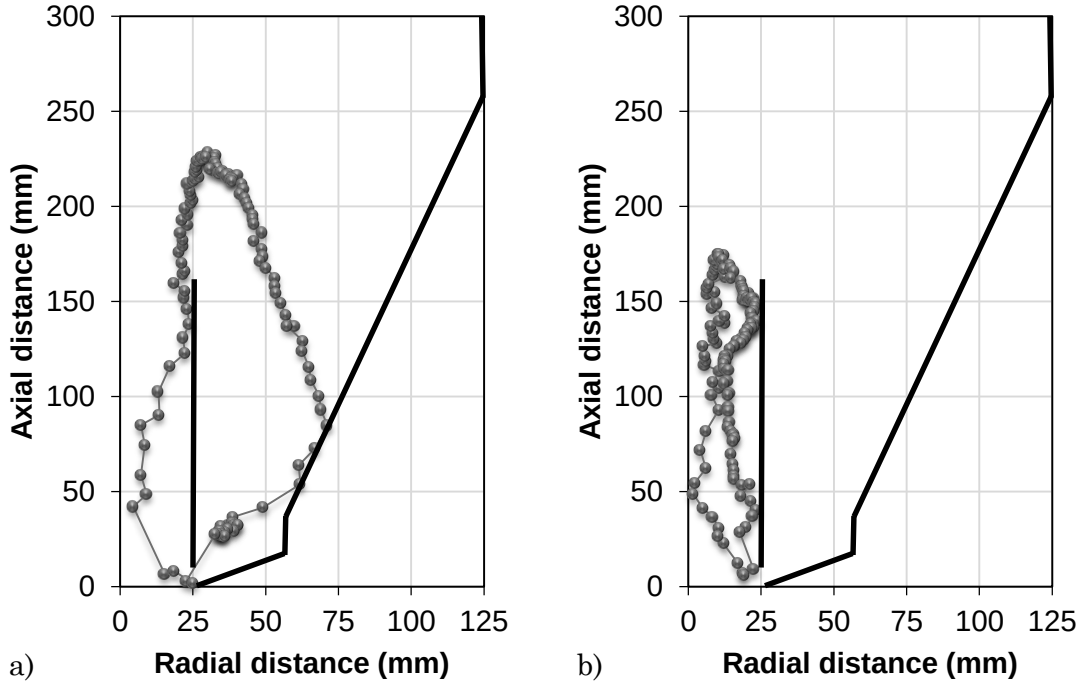


*Figure 5.1 Different types of trajectories: (a) cycle, and (b) recirculation. The bold lines are the walls of the fluidized bed and the Wurster tube.*

As described in the last section, a sequence of locations of the tracer particle was stored in each PEPT run. By following the location of the tracer particle over time, two types of trajectories can be defined:

a. Cycle (Figure 5.1a): the tracer particle departs from the spray zone, accelerates in the Wurster tube, and returns to the spray zone after passing through the fountain, downbed and horizontal transport regions.
b. Recirculation (Figure 5.1b): the tracer particle recirculates within the Wurster tube without passing through the downbed region. This type of trajectory is not desired because it is believed to increase the risk for

agglomeration of particles and to give a broader film thickness distribution.

It is noted that since it was not possible to define a spray region in the PEPT experiments, a particle cycle begins when first appearing in the Wurster tube, rather than in the spray zone.

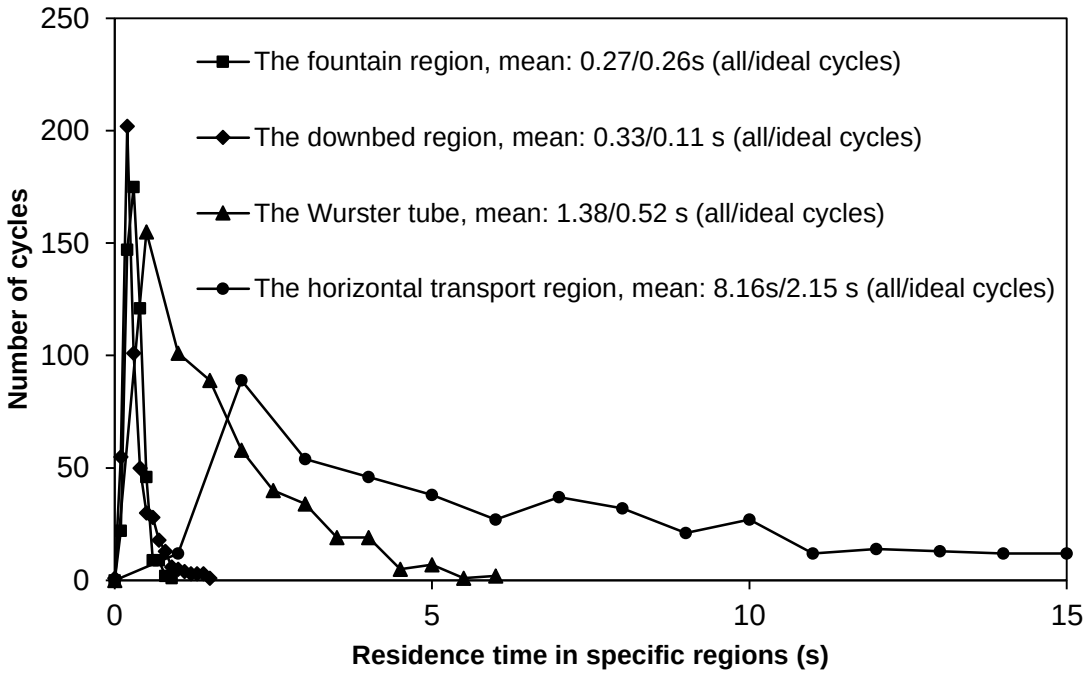


*Figure 5.2 Residence time distributions in specific regions, with mean values of all cycles and ideal cycles provided (partition gap 15 mm, batch size 200 g, particle VMD 1749 µm, tube length 150 mm, fluidization airflow rate 73.3 $m^3/h$, and atomization airflow rate 3.50 $m^3/h$), the bin size for the fountain and the downbed regions: 0.1 s, for the Wurster tube: 0.5 s, and for the horizontal transport region: 1 s.*

In a real coating process, it is desirable to minimize particle recirculations. Nevertheless, it was observed in the PEPT experiments that the particle tends to recirculate in the Wurster tube. When a cycle does not have any recirculation, it is regarded as an ideal cycle, otherwise it is non-ideal.

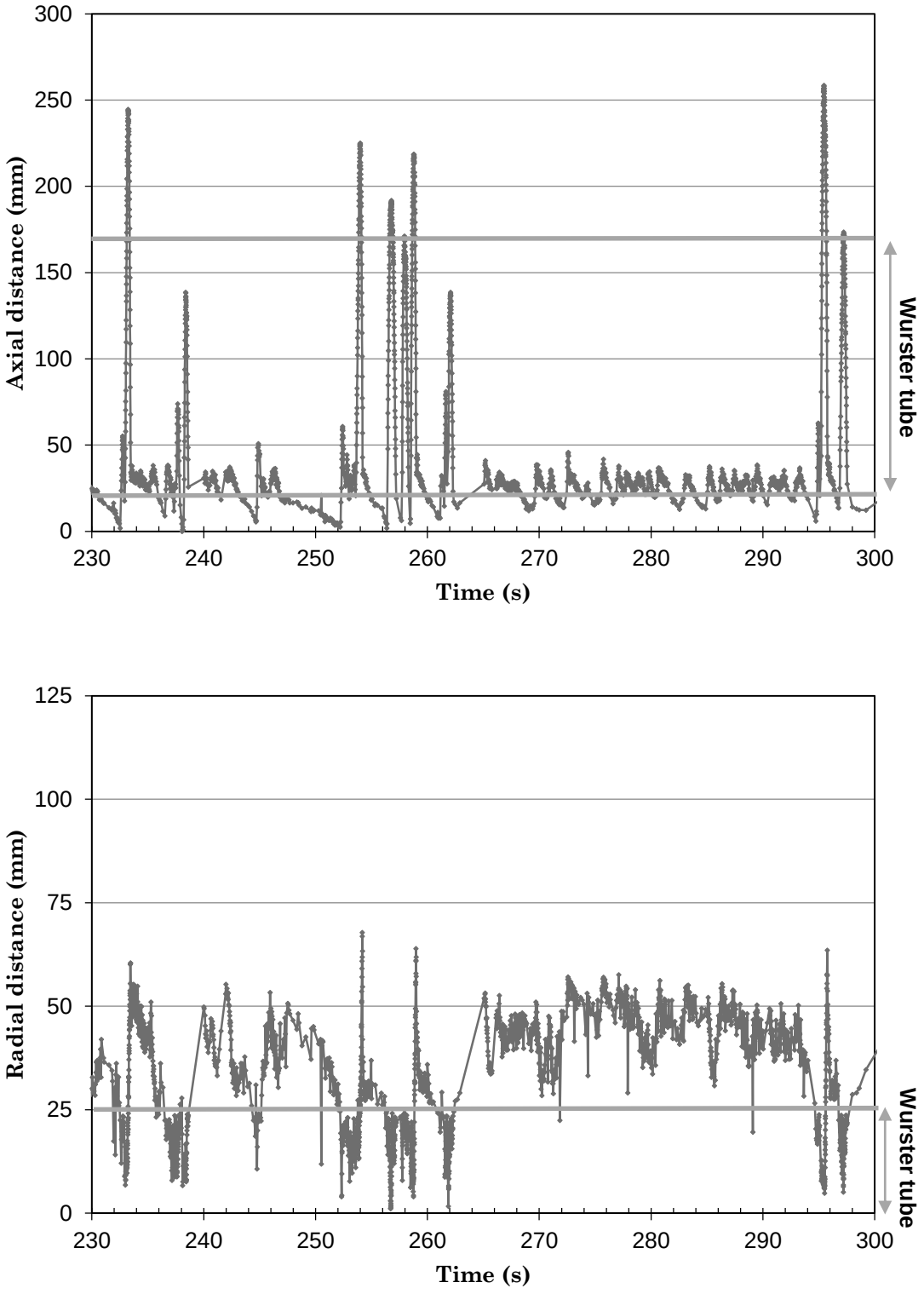


*Figure 5.3 An example of the axial (above) and radial (below) position of a tracer particle during 70 s.*

Figure 5.2 shows the RTDs of particles in different regions from all cycles and ideal cycles. It can be seen that the particle on average spends the longest time,

8.16 s, in the horizontal transport region, while it spends a much shorter time, 1.38 s, 0.27 s, and 0.33 s in the Wurster tube and in the fountain and downbed regions, respectively. Moreover, the residence time in the Wurster tube and particularly in the horizontal transport region is much shorter for the ideal cycles than for all cycles. In principle, the main difference between ideal and non-ideal cycles is the particle recirculation that occurs in the Wurster tube. However, it was found that the very long residence time in the horizontal transport region for non-ideal cycles most likely is a result of the particle returning to the horizontal transport region by passing out of the Wurster tube through its lower edge. This conclusion is supported by an example of particle trajectory during the 230-300 s as shown in Figure 5.3, more specifically at 238 s and 263 s.

More effects, such as the effects of the partition gap, the batch size, the length of the Wurster tube, the fluidization and atomization airflow rates, and binary mixtures on pellet motion were also investigated in Paper I. For a given piece of equipment, it was found that it is possible to optimize the partition gap so that it is small enough to direct the fluidization airflow into the Wurster tube and large enough not to limit the solids flux into the tube. It was also observed that, as the batch size increases, the cycle time decreases and the CTD becomes narrower. This implies that it is possible to coat a larger batch of pellets in a shorter amount of time and while ensuring less variability in the coating film thickness. Nevertheless, this may be limited by the spray rate since a higher spray rate then is required for a larger batch. This, however, suggests opportunities to establish more efficient processes by exploring higher spray rates for larger batches.

For binary mixtures of small and large pellets, it was found that large pellets have a longer cycle time than small pellets, which indicates that smaller pellets

get coated more frequently. Nevertheless, it was not clear in previous work (Sudsakorn & Turton, 2000; Paulo Filho *et al.*, 2006; Cahyadi *et al.*, 2012; Marucci *et al.*, 2012) whether large pellets would receive a higher total amount of coating mass than small pellets because large pellets circulated more often or because large pellets received more coating when they passed through the spray zone. The result here clearly provides evidence for the latter effect.

## 5.2. Validation and development of DEM-CFD model (Paper II)

### 5.2.1. Calibration of inlet flow

As mentioned earlier, the velocity at the inlet boundary at the distributor is determined by fluidization airflow and the velocity at the nozzle depends on atomization airflow. For fluidization airflow, which has a major effect on how the particles behave in the fluidized bed (Li *et al.*, 2016), it is necessary to specify airflow distribution. Since it was not possible to experimentally measure airflow distribution, several DEM-CFD simulations using various flow distributions were performed. The resulting particle velocities at different heights were compared with the PEPT measured values. Then the flow distribution, under which the adequate agreement between the calculated and measured particle velocity, was achieved is defined as the inlet boundary condition for the DEM-CFD simulations.

Moreover, in order to ensure that the flow distribution at the distributor obtained via the comparison of the calculated and measured particle velocity is reasonable, a CFD model for single-phase airflow was developed. This CFD model gives the fractions of the fluidization airflow passing though the central region of the distributor and through the outer annulus region. This single-phase

CFD model includes the air supply chamber, the bowl-shaped distributor with orifices, the wire mesh screen and the fluidized bed. More details on this single-phase model are provided in the Appendix.

### 5.2.2. Model validation

In order to evaluate the DEM-CFD model for particle motion, a simulation for the base case was carried out. Particle motion was investigated in detail with respect to the particle velocity, and the CTD and the RTD of particles in different regions.

In Figure 5.4, the particle velocity field given by the DEM-CFD simulation and measured using the PEPT experiment shows good qualitative agreement. Quantitatively, as shown in Figure 5.5 and Figure 5.6, there is also good agreement between the calculated and measured CTD and between the calculated and measured mean residence times of particles in different regions.

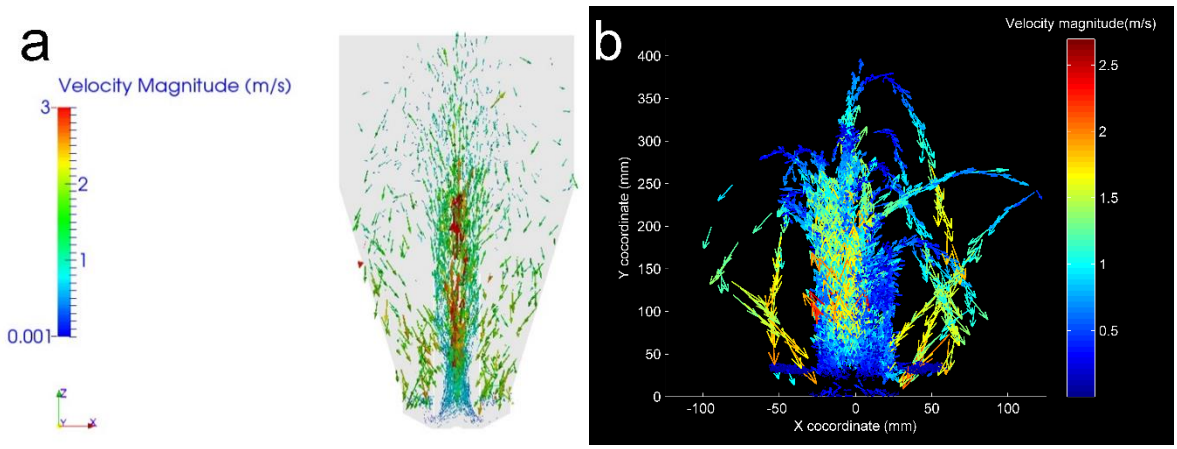


*Figure 5.4 The particle velocity field at a vertical cross-section through the center of the bed (a) simulated using DEM-CFD and (b) measured using PEPT (VMD 1749 μm, batch size 200 g, fluidization airflow rate 73.3 $m^3/h$ and atomization airflow rate 3.50 $m^3/h$).*

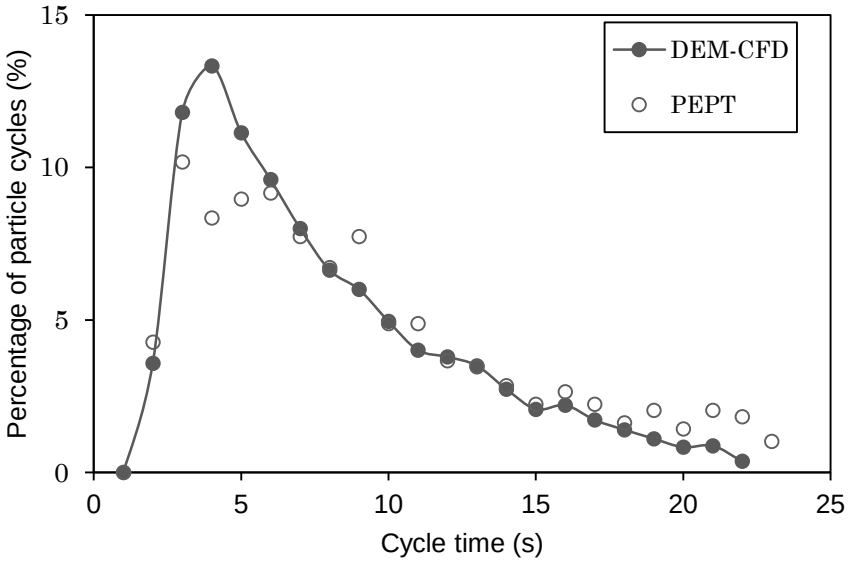


*Figure 5.5 The cycle time distribution (for cycles shorter than 25 s) calculated in the DEM-CFD simulation and measured in the PEPT experiment (VMD 1749 µm, batch size 200 g, fluidization airflow rate 73.3 m³/h and atomization airflow rate 3.50 m³/h).*

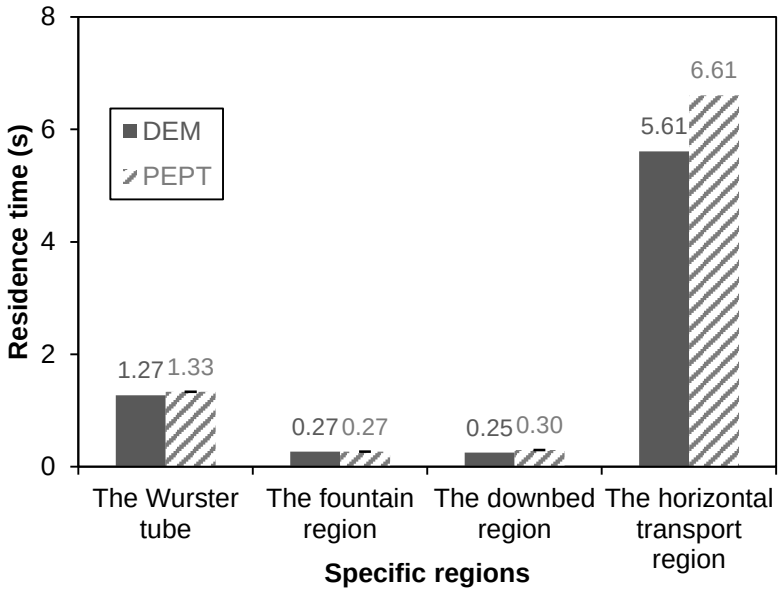


*Figure 5.6 The mean residence times of particles in different regions (VMD 1749 µm, batch size 200 g, fluidization airflow rate 73.3 m³/h and atomization airflow rate 3.50 m³/h).*

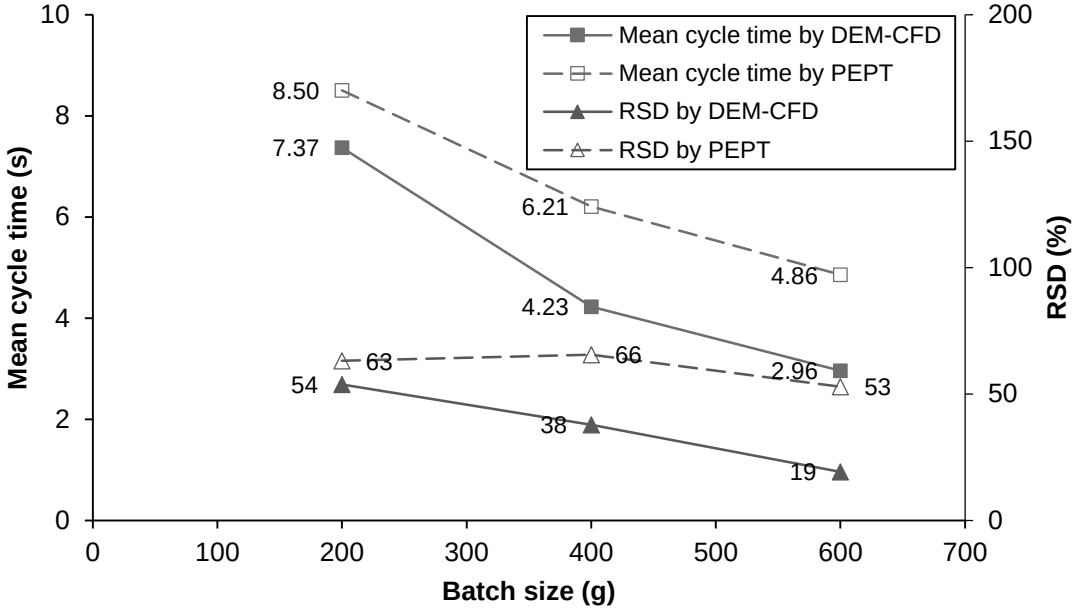


*Figure 5.7 The mean cycle time and RSD for different batch sizes (VMD 1749 μm, fluidization airflow rate 73.3 m³/h and atomization airflow rate 3.50 m³/h).*

Furthermore, as an interesting observation in the PEPT experiments, the cycle time, as well as the relative standard deviation (RSD), decreases when the batch sizes increases. This effect is beneficial to process operation since it suggests that larger batches can be coated with a more uniform coating thickness (i.e. better quality) faster. This phenomenon was further investigated using the DEM-CFD simulations, which show a similar trend, as illustrated in Figure 5.7. This effect can be attributed to the fact that for the increased batch size, particles accelerate faster in the Wurster tube, which gives fewer particle recirculations and less cycle time.

Although the absolute values of cycle time and the RSD for each batch size still exhibit slight differences between the experiments and the simulations, it can be concluded that the DEM-CFD model for particle motion works for the present system. A possible step forward for improvement would be to incorporate the actual PSD instead of the VMD in the DEM-CFD simulations or to consider the shape of the particles.

### 5.2.3. Evaluation of drag model (Paper III)

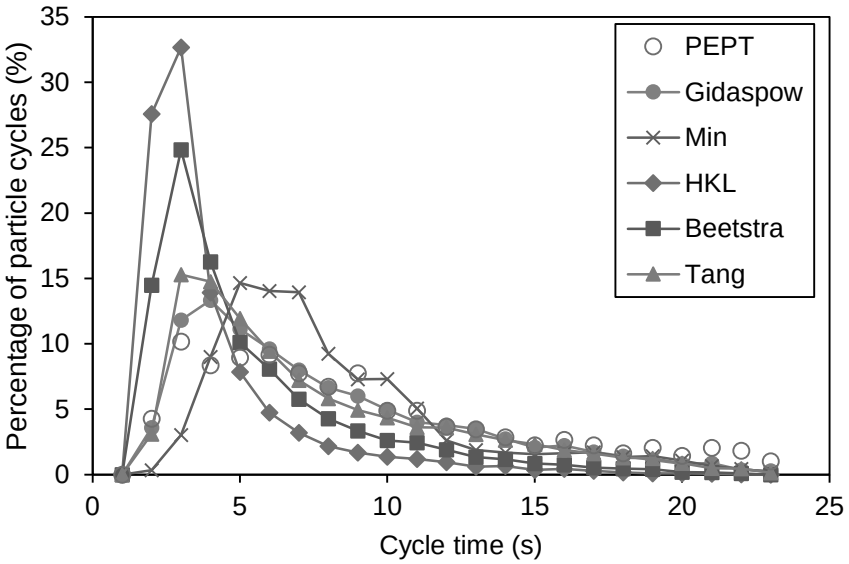


*Figure 5.8 The cycle time distribution of particle cycles shorter than 25 s (VMD 1749 µm, batch size 200 g, fluidization airflow rate 73.3 m³/h and atomization airflow rate 3.50 m³/h).*

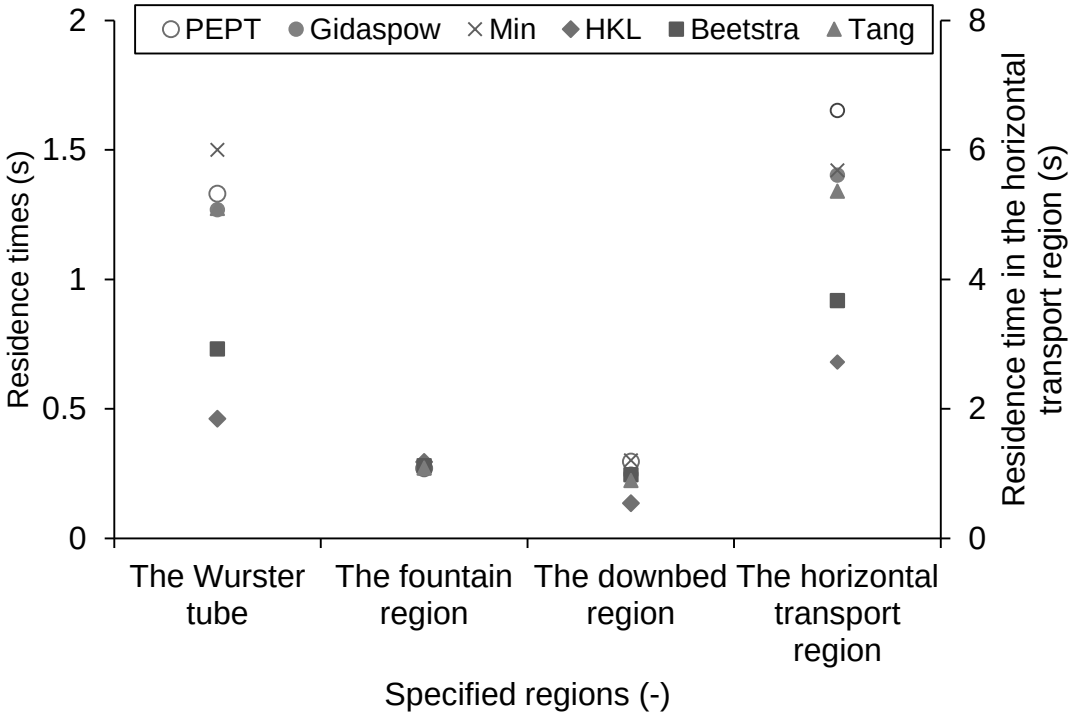


*Figure 5.9 The residence times of particles in different regions for the base case (VMD 1749 µm, batch size 200 g, fluidization airflow rate 73.3 m³/h and atomization airflow rate 3.50 m³/h).*

In order to determine if it is possible to improve the DEM-CFD model by refining the model for the interphase momentum transfer, four other drag models were examined. Figure 5.8 and Figure 5.9 show the CTD and the residence times of particles in different regions, respectively, from the DEM-CFD simulations using different drag models. When examining the particle velocity at different heights, only a slightly higher particle velocity in the Wurster tube was found for the HKL and Beetstra drag models. However, this slight difference in the particle velocity in the Wurster tube can result in a distinct difference in particle recirculations, i.e. due to particles sneaking out from below the lower edge of the Wurster tube.

A different number of particle recirculations certainly cause differences in the residence time of particles in the horizontal transport region and in the cycle time. Therefore, the predicted coating quality can depend to a great extent on the choice of drag models. Among these tested drag models, the one recently proposed by Tang *et al.* (2015) showed good agreement with the PEPT data (without any increase in computational cost) and should be considered in future work. The investigation here again emphasizes the significance of the detailed particle motion in the Wurster tube and suggests that care must be taken when selecting the drag model for similar fluidized beds.

## 5.3. A predictive model for growth of pellets (Paper II and Paper IV)

In order to understand the particle motion near the spray nozzle and how it can affect the coating process, a spray zone in the shape of a solid cone was defined as shown in Figure 5.10. This spray zone is mainly conceptual and is similar to

the one in the study by Fries *et al.* (2011). The height of the spray zone, $L$, is assumed to be 45 mm and the spray half-angle, $\theta$, is assumed to be 30 degrees.

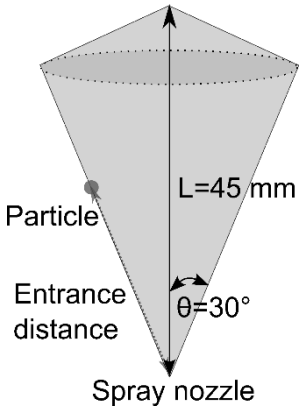


*Figure 5.10 A schematic of the spray zone.*

In order to shed light on the underpinning mechanisms of how pellets with a certain PSD grow differently during coating, mixtures of small and large pellets were studied. Parameters such as the cycle time, the residence time of particles in the spray zone and the entrance distance into the spray zone, i.e. the distance between the spray nozzle and the location where particles move into the spray zone (see Figure 5.10), were investigated. Among these parameters, the residence time of particles in the spray zone and the entrance distance were not available in the PEPT experiments, due to the poor data quality in this region. It was, however, possible to obtain all these parameters in the DEM-CFD simulations, but nonetheless time-consuming for the cycle time. Therefore, the cycle time was taken from the PEPT experiments while the RTD in the spray zone and the entrance distance into the spray zone were obtained from the DEM-CFD simulations.

In the PEPT experiments, it was found that large pellets have a longer mean cycle time than small pellets (c.f. Figure 5.11), which is equivalent to large pellets traveling less frequently through the spray zone. In addition, a smaller difference in cycle time was observed for the mixture with a larger fraction of

large pellets. On the other hand, the results obtained from the DEM-CFD simulations show that large pellets spend a longer time in the spray zone and move closer to the spray nozzle (c.f. Figure 5.12 and Figure 5.13). As the fraction of large pellets in mixtures increases, the difference in the residence time in the spray zone between the different mixtures increases accordingly.

Based on this data, the effects of the residence time in the spray zone, the entrance distance into the spray zone, the cycle time and the particle diameter on the coating thickness were explored with the predictive model described below.

The total amount of coating per unit time deposited on the surface of a particle, $m_{film}$, can be expected to be proportional to the spray rate, $\dot{m}$, the time spent in the spray zone, $t_{spray}$, and the number of coating cycles, $N_{cycle}$. The probability that a spray droplet is deposited onto a particle can be expected to be proportional to the cross-sectional area of the particle and to the droplet flux, which decreases quadratically with the distance from the spray nozzle for a solid-cone spray zone. Thus this model can be written as

$$\frac{dm_{film}}{dt} = K(r_{entrance})\dot{m}\left(\frac{t_{spray}}{t_{cycle}}\right)\left(\frac{\pi {d_p}^2/4}{{r_{entrance}}^2}\right) \qquad (5.1)$$

where $t_{cycle} \sim 1/N_{cycle}$ is the cycle time and $K$ represents other factors that may affect the amount of coating solution that a particle receives such as the shielding effect. Since the shielding effect is predominantly entrance distance dependent, $K$ should be a function of the entrance distance, i.e. $K \sim 1/r_{entrance}$. The rate of increase in the coating thickness can then be written as

$$\frac{dl_{film}}{dt} = \frac{1}{\rho_{film}\pi {d_p}^2}\frac{dm_{film}}{dt} \qquad (5.2)$$

where $\rho_{film}$ is the density of the coating film.

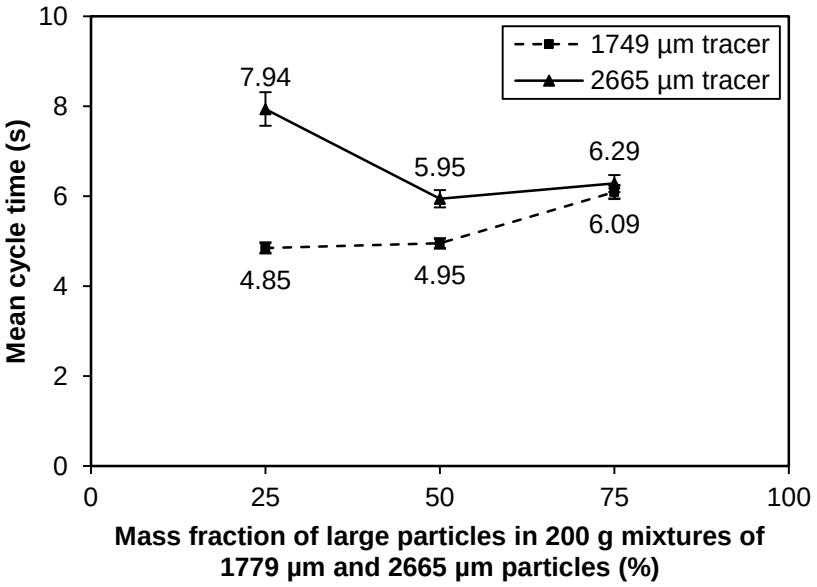


*Figure 5.11 The measured cycle time of small and large particles in the spray zone for different mixtures of small and large particles.*

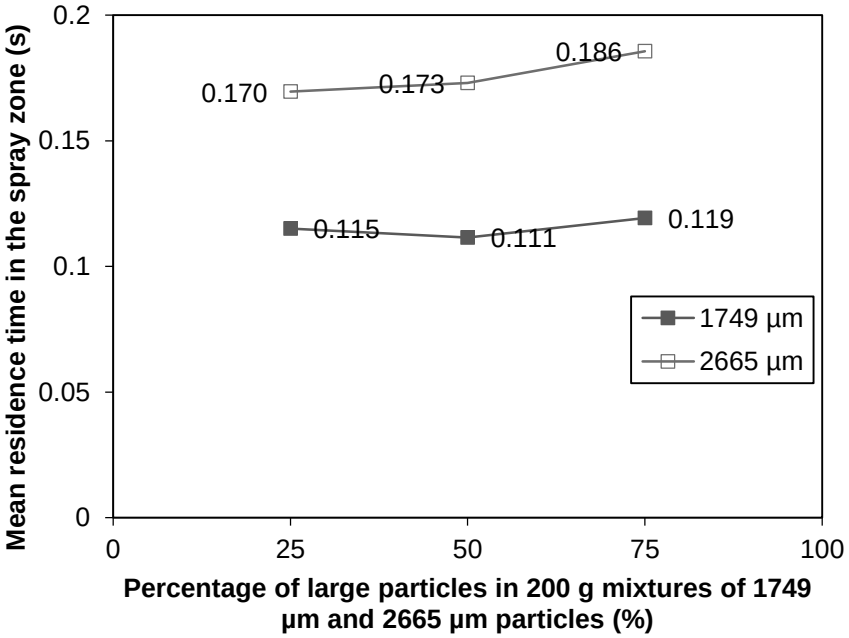


*Figure 5.12 The simulated residence time of small and large particles in the spray zone for different mixtures of small and large particles.*

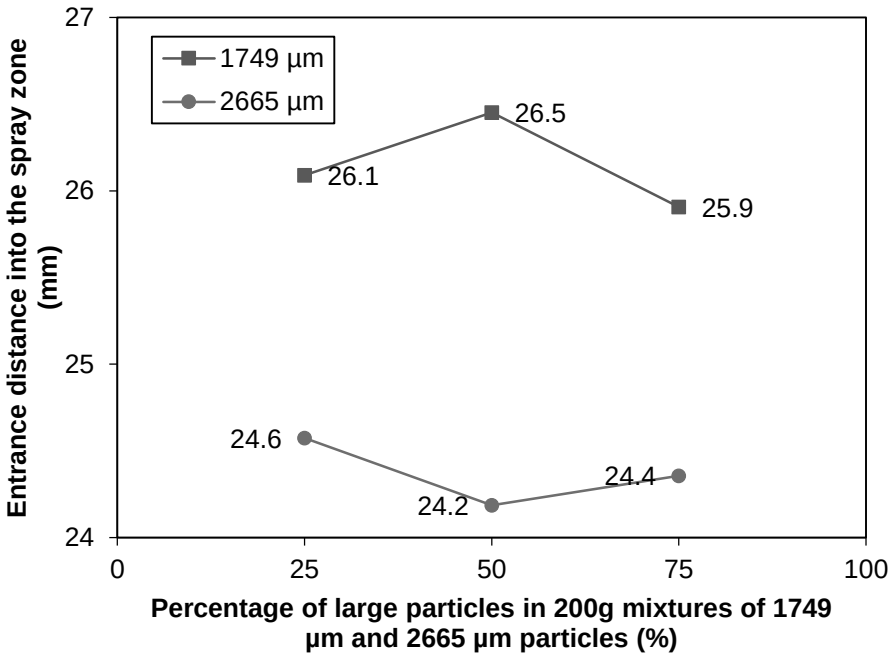


*Figure 5.13 The simulated entrance distance into the spray zone of small and large particles for different mixtures of small and large particles.*

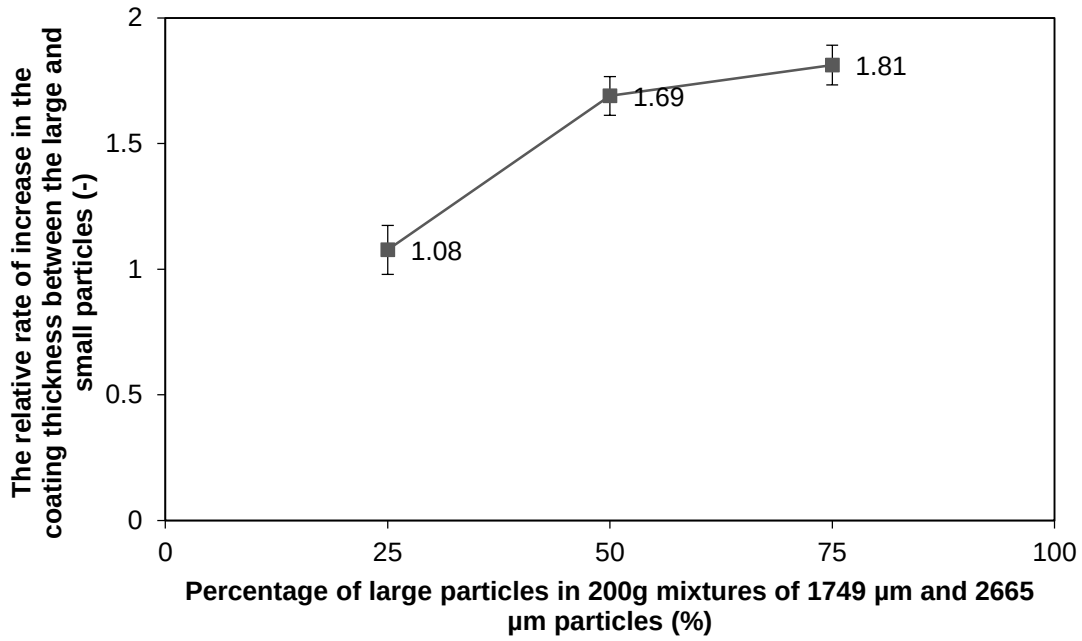


*Figure 5.14 The predicted relative rate of increase in the coating thickness between the large and small particles for different mixtures of small and large particles.*

Using the above model, it is straightforward to predict the relative rate of increase in the coating thickness between the large and small particles for different mixtures, as shown in Figure 5.14. As seen in Figure 5.14, large particles grow only slightly faster than small particles for the mixture with 25% large particles. In this mixture, the longer residence time in the spray zone and the closer entrance distance into the spray zone for larger particles are almost counteracted by their less frequent passes though the spray zone. As the fraction of large particles in the mixture increases, however, large particles show a greater rate of increase in the coating thickness. This is well supported by the fact that there is less difference in the cycle time (between large and small particles) and a greater difference in the residence time in the spray zone (between large and small particles).

*Table 5.1 The size of the coated small and large particles for different mixtures.*

| **Fraction of the large particles in the mixture (%)** | **Class of particles (-)** | **VMD (μm)** | **Growth (μm)** | **Relative rate of increase in the coating thickness between the large and small particles (-)** |
|---|---|---|---|---|
| **25** | Small | 1866 | 42 | |
| | Large | 2833 | 65 | 1.56 |
| **50** | Small | 1867 | 50 | |
| | Large | 2832 | 69 | 1.39 |
| **75** | Small | 1880 | 50 | |
| | Large | 2821 | 73 | 1.45 |

Although the predictive model is simple, the general understanding that it provides can be expected to be applicable to other similar pieces of equipment. Therefore, coating experiments using different equipment and a real two-fluid atomization nozzle were performed to evaluate the performance of this model. In these coating experiments, mixtures of the MCC pellets with the specifications given in Table 4.2 were coated with EC/HPC polymer films. Table 5.1 shows the

size of the small and large pellets after coating for the different mixtures. It can be seen that, during the same period of operation, large pellets had a greater rate of increase in the coating thickness than small pellets: 1.56, 1.39 and 1.45 for mixtures with 25%, 50% and 75% large pellets. The magnitude of these values is close to the prediction using the simple model and, additionally, clearly show that large pellets grow faster than small pellets.

Despite qualitative agreement between the model predictions and the experimental results, the trend of an increase in relative rate for the mixture with more large particles was not confirmed in these experiments. Possible refinements to include a more realistic representation of the equipment and to include different model assumptions as well as micro-level phenomena such as drying conditions in different regions are therefore suggested in Paper IV.

## 5.4. Particle drying

The experimental results, as can be seen in Paper V, are obtained for the mean temperature and moisture content in air measured at different locations of the fluidized bed. These results can be used for evaluating the performance of the model for particle drying by comparing the simulated and measured values of the temperature and moisture content in air at different locations. It is then possible to access the temperature and moisture content for individual particles at different times from the ongoing DEM-CFD simulations. In addition, the drying rate of particles in different regions of the fluidized bed can be obtained.

# 6. Conclusions and outlook

In this thesis, with the overall objective of developing a mathematical model for predicting the fluidized bed coating process, both experimental and modeling efforts were focused on understanding the mechanisms that affect the coating process. Overall, the following conclusions can be drawn.

A series of PEPT experiments were carried out to study particle motion in a laboratory-scale Wurster fluidized bed. The measured particle trajectories were used to identify particle cycles and to determine the CTD and the RTD of particles in different regions of the fluidized bed. The effects of the partition gap, the batch size, the Wurster tube length, and the fluidization and atomization airflow rates on the CTD and the RTD of particles in different regions were investigated. In this case, the experiments showed that particles spend most of the cycle time in the horizontal transport region and, on average, approximately 12–29% of the time in the Wurster tube. It was observed that particles tend to recirculate in the Wurster tube and sneak out from the bottom of the tube, particularly if the partition gap is large, if the atomization flow rate is low or if the Wurster tube is long. It was interesting to note that the cycle time decreased and the CTD became narrower as the batch size increased.

Based on the parameters used in the PEPT experiments, coupled DEM-CFD simulations were performed. The simulated particle trajectories were used to determine the particle velocity field, the CTD and the residence times of particles in different regions. The calculated results were then compared with the PEPT data. The general characteristic particle motion was successfully captured in the DEM-CFD simulations. The CTD and the residence times of particles in different regions were found to correspond closely to the experimental results. A shorter

cycle time with a larger batch size was also predicted by the DEM-CFD simulations.

In addition, in an effort to refine the model by examining different drag models, it was found that satisfactory agreement could be obtained using the Gidaspow and the Tang drag models. The agreement between the model predictions and the experimental data leads to the conclusion that the DEM-CFD model for particle motion is valid for the current system.

Using the validated DEM-CFD model, the detailed particle motion in a simplified spray zone was studied for particles of different sizes. The results showed that large particles spend a longer time in the spray zone and, on average, move closer to the spray nozzle. Large particles obviously receive a greater amount of coating solution due to their larger size, but the fact that they travel closer to the spray nozzle than small particles provides evidence that large particles can shield small particles from spray droplets. Both of these effects suggested that large particles receive a greater amount of coating solution per cycle than small particles. This, however, is partly counteracted by the fact that large particles pass through the spray zone less frequently than small particles.

A simple conceptual model was then developed to predict the effect of the residence time of particles in the spray zone, the cycle time, and the entrance distance on the relative rate of increase in film thickness between large and small particles. In addition, coating experiments were performed for evaluation of the performance of this model. On comparing predicted and measured relative rates of increase in coating thickness between large and small particles, a qualitative agreement was obtained. It was confirmed that large particles grow faster than small particles. Due to the simplicity of the model, several refinements were suggested.

In a first model attempt, a model for particle drying was developed. Drying experiments for parameter values similar to the ones used for the DEM-CFD simulations were carried out to evaluate the performance of the model. Then it is possible to access the temperature and moisture content for individual particles at different times, as well as the drying rate of particles in different regions of the fluidized bed, from the ongoing DEM-CFD simulations.

In all, this study demonstrates the power and potential of DEM as an important tool for mechanistic studies of pellet coating in fluidized beds. Further steps forward include the following. First, a better description of the atomization airflow for real atomization nozzles is of interest. Although the simple model for droplet deposition developed here was found to work quite well, it is nevertheless of interest to gain a better understanding of the motion of particles and spray droplets in the vicinity of the atomization nozzle. From a computational perspective, this is challenging since it involves droplet breakup as well as effects due to turbulence. Second, PSDs and possibly also the sphericity of particles may be considered in further study. Third, it is also of interest to incorporate other mechanisms into the model, such as agglomeration due to collisions between wet particles and/or electronic charging. In addition, a reduction in the computational cost would obviously also be very beneficial in order to handle similar amounts of smaller particles or bigger batches of large particles. In the end, it is of significance to tie all individual contributing mechanisms together in order to further improve the predictive model that is in a multiscale nature.

# References


Bommisetty, R. V. N., Joshi, D. S., & Kollati, V. R. (2013). Flow Loss in Screens: A Fresh Look at Old Correlation. *Journal of Mechanics Engineering and Automation, 3*(1), 29-34.

Bruchmüller, J. (2011). *Modelling the degradation of particles in fluidised beds.* (Doctoral), University of Southampton, PhD thesis. Retrieved from http://eprints.soton.ac.uk/333308/

Bruchmüller, J., Gu, S., Luo, K. H., & Van Wachem, B. G. M. (2010). Discrete element method for multiscale modeling. *Journal of Multiscale Modelling, 02*(01n02), 147-162.

Cahyadi, C., Koh, J. J. S., Loh, Z. H., Chan, L. W., & Heng, P. W. S. (2012). A Feasibility Study on Pellet Coating Using a High-Speed Quasi-continuous Coater. *Aaps Pharmscitech, 13*(4), 1276-1286.

Capecelatro, J., & Desjardins, O. (2013). An Euler–Lagrange strategy for simulating particle-laden flows. *Journal of Computational Physics, 238*(0), 1-31.

Cheng, X. X., & Turton, R. (2000). The prediction of variability occurring in fluidized bed coating equipment. I. The measurement of particle circulation rates in a bottom-spray fluidized bed coater. *Pharmaceutical Development and Technology, 5*(3), 311-322.

Chiti, F. (2008). *Lagrangian studies of turbulent mixing in a vessel agitated by a rushron turbine: positron emission particle tracking (PEPT) and computational fluid dynamics (CFD).* (Ph.D.), University of Birmingham. Retrieved from http://etheses.bham.ac.uk/1607/

Chopra, R., Alderborn, G., Newton, J. M., & Podczeck, F. (2002). The influence of film coating on pellet properties. *Pharmaceutical Development and Technology, 7*(1), 59-68.

Christensen, F. N., & Bertelsen, P. (1997). Qualitative description of the Wurster-based fluid-bed coating process. *Drug Development and Industrial Pharmacy, 23*(5), 451-463.

Crowe, C. T., Schwarzkopf, J. D., Sommerfeld, M., & Tsuji, Y. (2012). *Multiphase Flows with Droplets and Particles, Second Edition*. GB: CRC Press Inc.

Cundall, P. A., & Strack, O. D. (1979). A discrete numerical model for granular assemblies. *Geotechnique, 29*(1), 47-65.

Darelius, A., Lennartsson, E., Rasmuson, A., Niklasson Björn, I., & Folestad, S. (2007). Measurement of the velocity field and frictional properties of wet masses in a high shear mixer. *Chemical Engineering Science, 62*(9), 2366-2374.

Deen, N. G., van Sint Annaland, M., van der Hoef, M. A., & Kuipers, J. A. M. (2007). Review of discrete particle modeling of fluidized beds. *Chemical Engineering Science, 62*(1-2), 28-44.

Dintwa, E., Tijskens, E., & Ramon, H. (2007). On the accuracy of the Hertz model to describe the normal contact of soft elastic spheres. *Granular Matter, 10*(3), 209-221.

Du, W., Bao, X., Xu, J., & Wei, W. (2006). Computational fluid dynamics (CFD) modeling of spouted bed: Assessment of drag coefficient correlations. *Chemical Engineering Science, 61*(5), 1401-1420.

Ergun, S. (1952). Fluid flow through packed columns. *Chemical Engineering Progress, 48*(2), 89-94.

Filho, R. S. C., Barrozo, M. A. S., Limaverde, J. R., & Ataide, C. H. (1998). Use of a spouted bed in the fertilizer coating of soybean seeds. *Drying Technology, 16*(9-10), 2049-2064.

Fries, L., Antonyuk, S., Heinrich, S., & Palzer, S. (2011). DEM–CFD modeling of a fluidized bed spray granulator. *Chemical Engineering Science, 66*(11), 2340-2355.

Gidaspow, D. (1994). *Multiphase flow and fluidization: continuum and kinetic theory description*. Boston: Academic.

Green, D. W., & Perry, R. H. (2008). *Perry's Chemical Engineers' Handbook (8th Edition)*: McGraw-Hill.

Gunn, D. J. (1978). Transfer of heat or mass to particles in fixed and fluidised beds. *International Journal of Heat and Mass Transfer, 21*(4), 467-476.

Hertz, H. (1882). Ueber die Berührung fester elastischer Körper. *Journal für die reine und angewandte Mathematik, 92*, 156-171.

Hrenya, C. M., & Sinclair, J. L. (1997). Effects of particle-phase turbulence in gas-solid flows. *AIChE Journal, 43*(4), 853-869.

Jajcevic, D., Siegmann, E., Radeke, C., & Khinast, J. G. (2013). Large-scale CFD–DEM simulations of fluidized granular systems. *Chemical Engineering Science, 98*(0), 298-310.

Jenike, A. W. (1961). Gravity Flow of Bulk Solids. *Bulletin No. 108, Utah State University*.

Jono, K., Ichikawa, H., Miyamoto, M., & Fukumori, Y. (2000). A review of particulate design for pharmaceutical powders and their production by spouted bed coating. *Powder Technology, 113*(3), 269-277.

Karlsson, S., Rasmuson, A., Niklasson Björn, I., & Schantz, S. (2011). Characterization and mathematical modelling of single fluidised particle coating. *Powder Technology, 207*(1–3), 245-256.

Karlsson, S., Rasmuson, A., van Wachem, B., & Niklasson Björn, I. (2009). CFD modeling of the Wurster bed coater. *AIChE Journal, 55*(10), 2578-2590.

Kearney, C. J., & Mooney, D. J. (2013). Macroscale delivery systems for molecular and cellular payloads. *Nat Mater, 12*(11), 1004-1017.

Kona, R., Qu, H., Mattes, R., Jancsik, B., Fahmy, R. M., & Hoag, S. W. (2013). Application of in-line near infrared spectroscopy and multivariate batch modeling for process monitoring in fluid bed granulation. *International Journal of Pharmaceutics, 452*(1–2), 63-72.

Li, L., Rasmuson, A., Ingram, A., Johansson, M., Remmelgas, J., von Corswant, C., & Folestad, S. (2015). PEPT study of particle cycle and residence time distributions in a Wurster fluid bed. *AIChE Journal, 61*(3), 756-768.

Li, L., Remmelgas, J., van Wachem, B. G. M., von Corswant, C., Johansson, M., Folestad, S., & Rasmuson, A. (2015). Residence time distributions of different size particles in the spray zone of a Wurster fluid bed studied using DEM-CFD. *Powder Technology, 280*(0), 124-134.

Li, L., Remmelgas, J., Wachem, B. G. M. v., Corswant, C. v., Folestad, S., Johansson, M., & Rasmuson, A. (2016). Effect of Drag Models on Residence Time Distributions of Particles in a Wurster Fluidized Bed: a DEM-CFD Study. *KONA Powder and Particle Journal,* 10.14356/kona.2016008.

Mallouppas, G., & van Wachem, B. (2013). Large Eddy Simulations of turbulent particle-laden channel flow. *International Journal of Multiphase Flow, 54*(0), 65-75.

Mann, V., & Crosby, E. (1975). Cycle time distribution measurements in spouted beds. *Canadian Journal of Chemical Engineering, 53*(5), 579-581.

Marucci, M., Holmgren, A., Carlsson, H., Jarke, A., Johansson, M., & von Corswant, C. (2012). Non-Uniformity of Pellets Coating, Effect on the Dose Release Profile and How to Improve the Coating Process by Reducing the Electrostatic Charging of the Pellets. *Chemical and Biochemical Engineering Quarterly, 26*(4), 379-384.

Pandey, P., & Bindra, D. S. (2013). Real-time monitoring of thermodynamic microenvironment in a pan coater. *Journal of Pharmaceutical Sciences, 102*(2), 336-340.

Parker, D. J., Allen, D. A., Benton, D. M., Fowles, P., McNeil, P. A., Tan, M., & Beynon, T. D. (1997). Developments in particle tracking using the Birmingham Positron Camera. *Nuclear Instruments and Methods in Physics Research Section A: Accelerators, Spectrometers, Detectors and Associated Equipment, 392*(1–3), 421-426.

Parker, D. J., Broadbent, C. J., Fowles, P., Hawkesworth, M. R., & McNeil, P. (1993). Positron emission particle tracking - a technique for studying flow within engineering equipment. *Nuclear Instruments and Methods in Physics Research Section A: Accelerators, Spectrometers, Detectors and Associated Equipment, 326*(3), 592-607.

Parker, D. J., Forster, R. N., Fowles, P., & Takhar, P. S. (2002). Positron emission particle tracking using the new Birmingham positron camera. *Nuclear Instruments and Methods in Physics Research Section A: Accelerators, Spectrometers, Detectors and Associated Equipment, 477*(1–3), 540-545.

Paulo Filho, M., Rocha, S. C. S., & Lisboa, A. C. L. (2006). Modeling and experimental analysis of polydispersed particles coating in spouted bed. *Chemical Engineering and Processing: Process Intensification, 45*(11), 965-972.

Rhie, C. M., & Chow, W. L. (1983). Numerical study of the turbulent flow past an airfoil with trailing edge separation. *AIAA Journal, 21*(11), 1525-1532.

Seville, J. (2010). *A single particle view of fluidization.* Paper presented at the The 13th International Conference on Fluidization - New Paradigm in Fluidization Engineering.

Shelukar, S., Ho, J., Zega, J., Roland, E., Yeh, N., Quiram, D., Nole, A., Katdare, A., & Reynolds, S. (2000). Identification and characterization of factors controlling tablet coating uniformity in a Wurster coating process. *Powder Technology, 110*(1), 29-36.

Sudsakorn, K., & Turton, R. (2000). Nonuniformity of particle coating on a size distribution of particles in a fluidized bed coater. *Powder Technology, 110*(1–2), 37-43.

Tang, Y., Peters, E. A. J. F., Kuipers, J. A. M., Kriebitzsch, S. H. L., & van der Hoef, M. A. (2015). A new drag correlation from fully resolved simulations of flow past monodisperse static arrays of spheres. *AIChE Journal, 61*(2), 688-698.

Teunou, E., & Poncelet, D. (2002). Batch and continuous fluid bed coating – review and state of the art. *Journal of Food Engineering, 53*(4), 325-340.

Tsuji, Y., Kawaguchi, T., & Tanaka, T. (1993). Discrete particle simulation of two-dimensional fluidized bed. *Powder Technology, 77*(1), 79–87.

Tsuji, Y., Tanaka, T., & Ishida, T. (1992). Lagrangian numerical simulation of plug flow of cohesionless particles in a horizontal pipe. *Powder Technology, 71*(3), 239-250.

Turton, R. (2008). Challenges in the modeling and prediction of coating of pharmaceutical dosage forms. *Powder Technology, 181*(2), 186-194.

Wen, C., & Yu, Y. (1966). Mechanics of Fluidization. *Fluidization, Chemical Engineering Progress Symposium Series 62*, 100-111.

Wurster, D. E. (1959). Air-suspension technique of coating drug particles. A preliminary report. *Journal of the American Pharmaceutical Association, 48*(8), 451-454.

# Appendix: Flow distribution at the distributor

In order to estimate the flow distribution at the distributor, which was unfortunately not possible to measure in the PEPT experiments, a single-phase CFD model was developed and is described as follows.

A 1/6$^{th}$ model of the Strea-1 fluid bed was considered including the wire mesh screen and the distributor. The detailed geometry of the screen was not included. Instead, the wire mesh screen was modeled as a region with a specified pressure loss. In Ansys Fluent, the CFD code used for this purpose, this was done using a porous zone model, as sketched in Figure A.1.

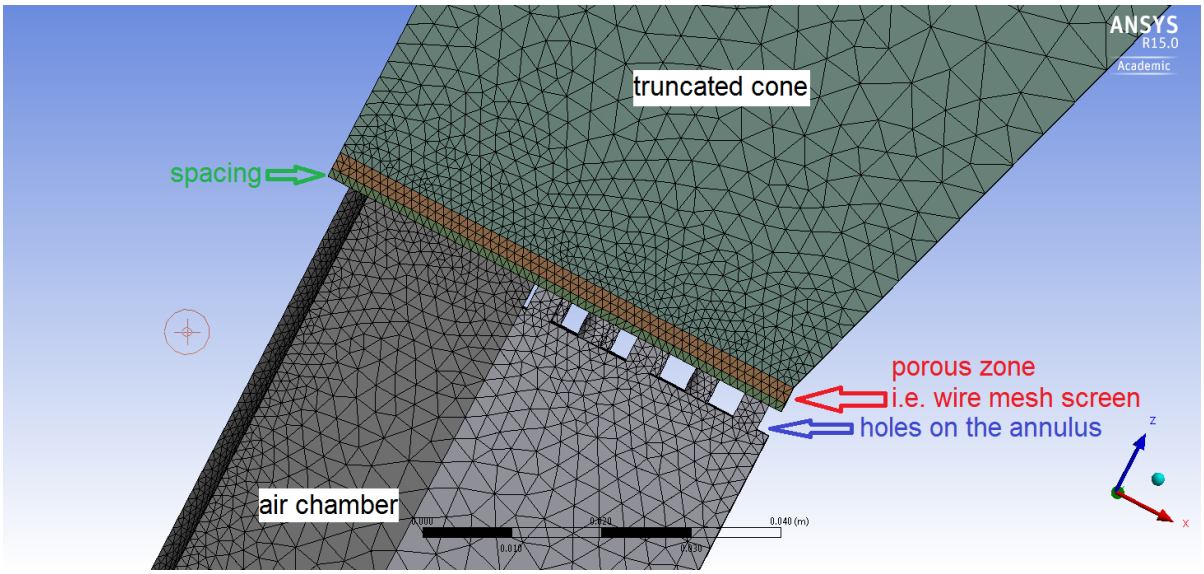


*Figure A.1 A 1/6$^{th}$ model of the Strea-1 fluidized bed, including the wire mesh screen as a porous zone.*

The pressure drop through the porous zone, i.e. the wire mesh screen, was modeled as an inertial resistance and calculated using (Green & Perry, 2008; Bommisetty *et al.*, 2013)

$$PD = \frac{1}{2} B \rho_g \boldsymbol{u}_g{}^2 \qquad (A.1)$$

where $B$ is the inertial resistance coefficient,

$$B = \frac{D}{l_p} \qquad (A.2)$$

In equation (A.2), $l_p$ is the thickness of the porous zone and $D$ is the pressure loss coefficient, which can be expressed by

$$D = \frac{1}{C^2}\left(\frac{1-\varepsilon^2}{\varepsilon^2}\right) \qquad (A.3)$$

where ε is the porosity and $C$ is the so-called discharge coefficient. The porosity is based on the ratio of the opening to the projected total area of the wire mesh screen and typically ranges from 0.14 to 0.79; for the screen employed here, its value was 0.36. The discharge coefficient is a function of the screen Reynolds number, $N_{Re}$, and may be written as

$$C = 0.1\sqrt{N_{Re}} \qquad (A.4)$$

where $N_{Re} = D_s u_g \rho_g / (\alpha \mu_g)$ and $D_s$ is the aperture width. For the screen used in the experiment, $D_s = 0.25\, mm$.

In the PEPT experiments, there was a certain spacing between the distributor and the wire mesh screen, as shown in Figure A.1. This spacing varied from 3 to 5 mm. The result, as shown in Figure A.2, shows that a larger spacing between the distributor and the wire mesh screen leads to less air to flow through the central base of the distributor. For the spacing that corresponds to the PEPT experiments, the airflow passing through the central base of the distributor was found to be between 52.9% and 63.5% of the total fluidization airflow.

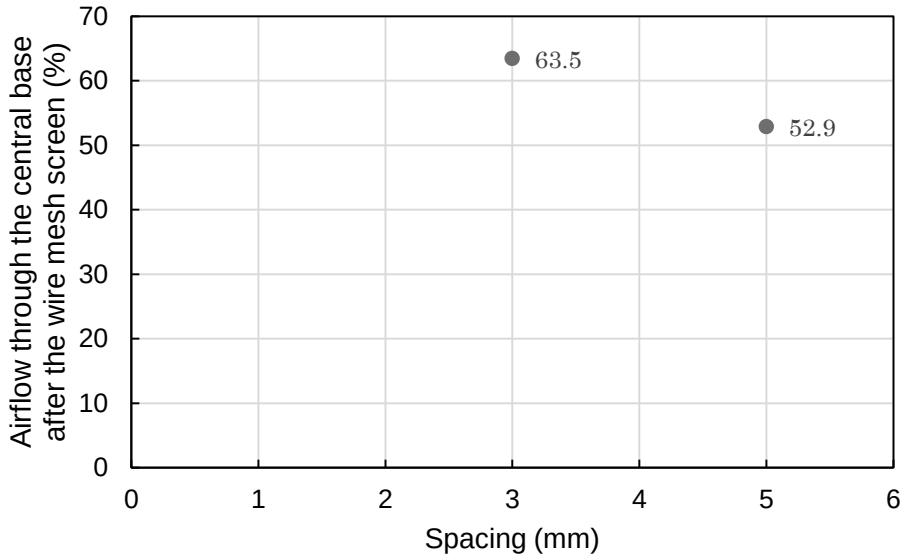


*Figure A.2 The percentage of total airflow passing through the central base of the distributor after the porous zone, i.e. the wire mesh screen, with a spacing of 3 mm and 5 mm.*